HHS Public Access

Author manuscript

Cancer Discov. Author manuscript; available in PMC 2024 June 12.

Published in final edited form as:

Cancer Discov. 2023 December 12; 13(12): 2652–2673. doi:10.1158/2159-8290.CD-22-1467.

Oncogenic KRAS drives lipo–fibrogenesis to promote angiogenesis and colon cancer progression

Wen-Hao Hsu[1], **Kyle A. LaBella**[1], **Yiyun Lin**[2], **Ping Xu**[2], **Rumi Lee**[1], **Cheng-En Hsieh**[3], **Lei Yang**[2], **Ashley Zhou**[1], **Jonathan M. Blecher**[1], **Chang-Jiun Wu**[4], **Kangyu Lin**[5], **Xiaoying Shang**[1], **Shan Jiang**[1], **Denise J. Spring**[1], **Yan Xia**[1], **Peiwen Chen**[1], **John Paul Shen**[5], **Scott Kopetz**[5], **Ronald A. DePinho**[1]

[1.]Department of Cancer Biology, The University of Texas MD Anderson Cancer Center, Houston, TX 77030, USA

[2.]Department of Genetics, The University of Texas MD Anderson Cancer Center, Houston, TX 77030, USA

[3.]Department of Immunology, The University of Texas MD Anderson Cancer Center, Houston, TX 77030, USA

[4.]Department of Genomic Medicine, The University of Texas MD Anderson Cancer Center, Houston, TX 77030, USA

[5.]Department of Gastrointestinal Medical Oncology, Division of Cancer Medicine, The University of Texas MD Anderson Cancer Center, Houston, TX 77030, USA

Abstract

Oncogenic KRAS (KRAS*) contributes to many cancer hallmarks. In colorectal cancer (CRC), KRAS* suppresses anti–tumor immunity to promote tumor invasion and metastasis. Here, we uncovered that KRAS* transforms the phenotype of carcinoma-associated fibroblasts (CAFs) into lipid–laden CAFs, promoting angiogenesis and tumor progression. Mechanistically, KRAS* activates the transcription factor CP2 (TFCP2) which upregulates the expression of the pro–adipogenic factors BMP4 and WNT5B, triggering the transformation of CAFs into lipid–rich CAFs. These lipid-rich CAFs, in turn, produce vascular endothelial growth factor A (VEGFA) to spur angiogenesis. In KRAS*–driven CRC mouse models, genetic or pharmacological neutralization of TFCP2 reduced lipid-rich CAFs, lessened tumor angiogenesis, and improved overall survival. Correspondingly, in human CRC, lipid-rich CAF and TFCP2 signatures correlate

Correspondence: Dr. Ronald A. DePinho, Department of Cancer Biology, The University of Texas MD Anderson Cancer Center, 1881 East Road, Unit 1906, Houston, TX 77054-1901, USA. rdepinho@mdanderson.org; Tel: 832-751-9756; Fax: 713-745-7167.

AUTHOR CONTRIBUTIONS

The authors confirm contribution to the paper as follows – Conceptualization and Methodology: **Wen-Hao Hsu, Kyle A. LaBella, Peiwen Chen, Yan Xia, Scott Kopetz, and Ronald A. DePinho**; Investigation: **Wen–Hao Hsu, Kyle A. LaBella, Yiyun Lin, Ping Xu, Rumi Lee, Cheng-En Hsieh, Lei Yang, Ashley Zhou, Jonathan M. Blecher, Chang-Jiun Wu, Kangyu Lin, Xiaoying Shang, and Shan Jiang**; Software: **Wen-Hao Hsu, Kyle A. LaBella, Yiyun Lin, Chang-Jiun Wu, and Kangyu Lin**; Data curation and formal analysis: **Wen-Hao Hsu, Kyle A. LaBella, and Yiyun Lin**; Resources: **John Paul Shen and Scott Kopetz**; Writing-Original draft preparation: **Wen-Hao Hsu**; Visualization: **Wen-Hao Hsu**; Supervision: **Ronald A. DePinho**; Validation: **Wen-Hao Hsu, Denise J. Spring, and Ronald A. DePinho**; Writing-Reviewing and Editing: **Denise J. Spring and Ronald A. DePinho**

Conflict Of Interest: RAD holds equity as a founder and former advisor and/or director of Tvardi Therapeutics, Asylia Therapeutics, Stellanova Therapeutics and Sporos Bioventures. The work of this study does not relate to these entities.

with worse prognosis. This work unveils a new role for KRAS* in transforming CAFs, driving tumor angiogenesis and disease progression, providing an actionable therapeutic intervention for KRAS*–driven CRC.

Keywords

Colorectal cancer; KRAS; lipid–rich CAFs; angiogenesis

INTRODUCTION

Colorectal cancer (CRC) is responsible for over 50,000 deaths in the United States and 600,000 deaths globally each year (1, 2). Although the 5–year survival rate is 90% for localized CRC, it is a dismal 14% for advanced metastatic disease (3). The signature genetic alterations of CRC include activating oncogenic mutations in *KRAS* (42%) and inactivating mutations and/or deletions of *APC* (75%) and *TP53* (60%) tumor suppressors (4, TCGA-COAD). In human CRC, the most common activating KRAS mutation, $KRAS^{G12D}$, is a glycine to aspartic acid substitution at codon 12 that correlates positively with advanced disease (5) and shows high co–occurrence in primary and metastatic tumors, supporting a role for $KRAS^{G12D}$ in CRC progression (6). Correspondingly, studies of mice engineered with a doxycycline (DOX)–inducible $KRAS^{G12D}$ allele and conditional null alleles for *APC* and *P53* (designated “iKAP” mice) have established that $KRAS^{G12D}$ (hereafter denoted as KRAS*) represses anti–tumor immunity and drives increased invasive and metastatic disease (7, 8).

Current targeted growth factor receptor therapies, such as those aimed at epidermal growth factor receptor (EGFR), fibroblast growth factor receptor, and insulin–like growth factor 1 receptor, have shown limited clinical benefit in metastatic CRCs harboring KRAS*, consistent with the actions of KRAS* in regulating cell survival and proliferative signaling downstream of these growth factor receptors. Alternative strategies for KRAS*–driven CRC have embraced targeting the downstream pathways of KRAS* such as the phosphoinositide 3–kinase/mammalian target of rapamycin (mTOR) and KRAS*/MEK pathways. However, the inhibition of mTOR (9) or MEK (10) have failed to demonstrate meaningful clinical activity in KRAS*–driven CRC patients, suggesting the presence of alternative or redundant KRAS* signaling pathways. Consistent with the redundancy thesis, combined MEK inhibitor (binimetinib), BRAF inhibitor (encorafenib), and EGFR inhibitor (cetuximab) treatment has shown increased clinical benefit in CRC patients with the $BRAF^{V600E}$ mutant, although recurrence still occurs in most cases, and treatment only extends the median survival duration by 3.6 months (11). The complexity of KRAS* function in CRC biology has been further substantiated by the discovery that KRAS* suppresses anti–tumoral immunity via the recruitment of myeloid–derived suppressor cells (8). While new therapies directly targeting KRAS* (e.g., adagrasib and sotorasib) show promising anti–tumor activity, the tumors of patients treated with these therapies rapidly acquire bypass mechanisms of resistance (12), underscoring the need to better understand the KRAS* signaling network to identify alternative or synergistic therapeutic interventions for KRAS*–driven CRC patients.

These continuing challenges prompted further exploration of the function of KRAS* in CRC tumor biology, particularly its impact on the host cells of the tumor microenvironment, such as immune cells, endothelial cells, and cancer–associated fibroblasts (CAFs). CAFs are among the most abundant, albeit the least understood and characterized, cells in the tumor microenvironment. CAF subtypes can be identified by markers, including alpha smooth muscle actin (αSMA), fibroblast–activation protein, and platelet–derived growth factor receptor (PDGFR). Myofibroblastic CAFs (αSMA+) and non–myofibroblastic CAFs (αSMA−) appear to be the most consistently defined subtypes present across diverse cancers (13-16). Myofibroblasts are lipid–sparse cells that transdifferentiate from adipocytes or lipofibroblasts (17, 18). CAF subtypes play opposing roles in the promotion or suppression of cancer (19, 20). Specifically, αSMA+ fibroblasts suppress Lgr5+ cancer stem cells and restrain CRC progression (21). Conversely, αSMA− CAFs secrete lipid metabolites into the tumor microenvironment via fatty acid translocase, thus promoting CRC metastasis by enhancing membrane fluidity (22, 23).

Mounting evidence suggests that specific cancer genotypes can influence CAF biology (24). For instance, P53 loss activates JAK2–STAT3 signaling to drive stromal fibrogenesis and promote tumor growth (25). KRAS*–induced sonic hedgehog (SHH) secretion shapes stromal cells to initiate reciprocal signaling of KRAS* via AXL/IGF1R–AKT signaling in pancreatic cancer (26). KRAS* reprograms pancreatic fibroblasts to activate inflammatory genes and polarize pro-tumorigenic macrophages (27). BRCA mutated cancer cells activate heat shock factor 1 (HSF1) in pancreatic stellate cells (PSCs), which transform into CLU^{+} immune regulatory CAFs (28). While KRAS* and other cancer genes can influence aspects of CAF biology, whether and how cancer cell oncogenic events influence CAF subtype biology and heterogeneity remains an area of active investigation.

In this study, our exploration of the biology and mechanisms of KRAS*–driven CRC progression revealed the capacity of KRAS* to transform the cell state of fibroblasts in the tumor microenvironment. We found that KRAS* activated the transcription factor CP2 (TFCP2) which directly upregulated transcription of pro-adipogenic cytokines, stimulating the phenotypic transformation of specific CAF subpopulations into lipid–rich CAFs that produced abundant vascular endothelial growth factor A (VEGFA) to promote angiogenesis and disease progression. In addition, the genetic or pharmacologic neutralization of TFCP2 impeded lipid–rich CAF development, blocked tumor angiogenesis, and inhibited tumor growth in KRAS*–expressing CRC. These insights, together with consonant human CRC profiles, provide a testable precision oncology therapeutic option for this intractable disease.

RESULTS

Lipid–rich CAFs are enriched in KRAS*–driven CRC

To identify pathways and processes that correlate with both KRAS* signaling and disease progression in CRC, we performed a gene set enrichment analysis (GSEA) of 19 bulk tumor RNA sequencing profiles to identify upregulated genes in iKAP murine tumors (in which KRAS* is present and functioning) compared with iAP (control) murine tumors (in which no KRAS* transgene is present) and in invasive primary tumors compared with noninvasive primary tumors. These intersected KRAS* and progression transcriptomes revealed

prominent representation of the adipogenesis pathway in invasive KRAS*–expressing CRC (Fig. 1A and S1A). These *in silico* findings aligned with tumor histology results, which showed a dramatic increase in lipid droplet abundance in the invasive iKAP tumor stroma compared to non-invasive iAP controls (Fig. 1B and S1B). Lipid-rich iKAP tumor stroma does not co-localize with αSMA and epithelial cellular adhesion molecule (CD326) staining (Fig. 1B); Lipid-rich iKAP tumor stroma colocalizes with delta–like homolog (DLK1), a marker of preadipocytes and lipid–rich fibroblast progenitors, further attesting to the adipocyte–like lineage enrichment in the stroma of KRAS*–expressing CRC (Fig. S1B). Flow cytometry analysis gated on LipidTOX$^+$, PDGFR alpha–positive (PDGFRα$^+$ [CD140a, a non-myofibroblast marker]), CD326$^-$ (a CRC epithelium marker), CD45$^-$ (an immune cell marker), and CD31$^-$ (an endothelial marker) cells revealed an increased percentage of lipid–rich CAFs in KRAS*–expressing invasive iKAP tumors compared with non-invasive iAP tumors (Fig. 1C and S1C). Immunohistochemical (IHC) and Western blot analyses corroborated the transcriptomic findings by confirming the enrichment of lipid droplets and adipocyte markers and regulators – DLK1, TCF21, PLIN4, FABP4, and LPL (29-31) – in KRAS*–expressing invasive iKAP tumors compared with non-invasive iAP controls; and the expression of fibroblast markers, COL3A1, THY1 and PDGFRα (Fig. 1D and S1D-E). To decipher KRAS–dependency and the stage–specificity of lipid–rich CAF enrichment during CRC development, we examined lipid–rich CAFs during tumor progression in high–, moderate– and low–grade invasive and non–invasive iKAP and iAP tumors. The intensity of positive lipid staining is more abundant in high-grade invasive iKAP tumors compared to moderate- and low-grade invasive and non-invasive iKAP and iAP tumors (Fig. 1E and S1F), indicating KRAS* and tumor stage dependency of lipid-rich CAF enrichment in CRC development.

To further characterize the KRAS*–driven stromal response, we conducted single–cell RNA sequencing (scRNA–seq) comparisons across invasive iKAP, non-invasive iAP, and non-invasive iKAP–DOXoff (KRAS*–off) CRC tumors. Among the 71,525 cells analyzed, 5984 stromal cells were identified, including (i) pericytes (RGS4− and RGS5–enriched), (ii) three endothelial cell (PECAM1− and ENG–enriched) subgroups, and (iii) six fibroblast (PDGFRα− and PDPN–enriched) subgroups (Fig. S2A). The fibroblast subtypes, including ECM$^+$ CAFs (COL12A1, COL1A2, and COL6A2); MMP$^+$ CAFs (MMP13, MMP10, and MMP9); PI16$^+$ CAFs (PI16, IL33, and CLIP); inflammatory CAFs (CXCL13, TNFSF13B, and C4B); proliferating fibroblasts; and myofibroblasts (ACTG2, TAGLN, and ACTA2) (Fig. 1F and S2A), were defined using previously established markers (32-36). Importantly, four CAF subgroups were notable for their expression of adipocyte– and/or adipogenesis–related genes (Fig. S2A, right). For example, ECM$^+$ CAFs express IGF1, which induces lipid production (37); MMP CAFs express Nrg1, which fine–tunes white adipose stem cell differentiation (38); PI16$^+$ CAFs express PI16$^+$, which is the marker of PDGFRα$^+$ adipocyte progenitor cells (39); and inflammatory CAFs express SFRP2, which enhances the adipogenic differentiation of dental mesenchymal stem cells (40). To validate these findings, we analyzed scRNA–seq data containing 2666 stroma cells from six KRAS mutant and six KRAS wild type tumors from CRC patients. These murine CAF annotations mirrored those in KRAS* and KRAS wild type human CRC, as reflected by scRNA–seq analyses showing six fibroblast subgroups including PI16$^+$, SFRP$^+$, inflammatory, extracellular

matrix (ECM), myofibroblasts and KI67$^+$ fibroblasts (Fig. S2B left). Moreover, the PI16$^+$, SFRP$^+$, inflammatory and ECM fibroblasts express adipocyte and/or adipogenesis–related genes, PI16, SFRP2, RARRES1, and SFRP4, respectively (41, 42) (Fig. S2B right).

Furthermore, we characterized the murine CAF subtypes corresponding to lipid–rich CAFs by using gene set module score analyses in murine scRNA datasets, which revealed that the adipocyte gene signature (43), and the combination of classic adipocyte and pre-adipocyte genes (29-31, 44, 45) were enriched in the 4 αSMA$^-$ CAF subgroups—inflammatory, PI16$^+$, ECM$^+$, and MMP$^+$ CAFs (Fig. 1F and S2C)—which express classic adipokine genes (DPT, DCN, and CCL2; Fig. S2D left) (44, 45) and lipid–rich fibroblast regulators and markers (TCF21, FGF10, PLIN3, and LPL; Fig. S2E left) (30). In contrast, αSMA$^+$ myofibroblastic CAFs show low or no expression of such signatures and markers, consistent with the lack of lipid droplets in this tumor–suppressive CAF subtype. Correspondingly, the same analyses of human CRC scRNA–seq revealed an adipocyte gene signature enriched in PI16$^+$ and SFRP$^+$ fibroblasts as well as adipokine genes and lipid–rich fibroblast markers (Fig. S2D-E right and S2F). Attesting to the scRNA–seq characterization of lipid–rich CAFs *in vivo*, transcriptomic analysis of flow–sorted, lipid–rich CAFs (LipidTOX$^+$/PDGFRα$^+$ and CD326$^-$/CD45$^-$/CD31$^-$) showed a lack of αSMA (ACTA2) expression and enrichment of the differential expression genes in the 4 CAF subgroups (Fig. 1G), reflecting the association between the lipid–rich fibroblast signature and the 4 αSMA$^-$ CAF subgroups.

Finally, scRNA–seq analysis showed increased lipid–rich CAFs (adipocyte gene signature and pre-/mature adipocyte genes are enriched in the combination of 4 αSMA− CAF subgroups, with the Pi16+ and inflammatory CAFs subtypes showing highest expression) in KRAS*–expressing invasive iKAP tumors compared with non-invasive iAP and KRAS*–off (no DOX) iKAP controls (Fig. 1F lower right panel, Fig. 1H, and S2G). These results aligned with the enrichment of lipid–rich CAFs (LipidTOX$^+$/PDGFRα$^+$) in KRAS*–expressing CRC tumors (Fig. 1C). These murine findings mirror those from KRAS* human CRC scRNA–seq data showing increased lipid–rich CAFs (PI16$^+$ and SFRP$^+$ fibroblasts) (Fig. S2H) and from the Cancer Genome Atlas (TCGA) analyses comparing *APC$^-$/P53$^-$/KRAS** versus *APC$^-$/P53$^-$/KRAS^{WT}* (Fig. S2I-M) showing a positive correlation between KRAS*–driven CRC and the lipid–rich CAF (αSMA−) gene signatures (Supplementary Table S1) (Fig. S2N). Together, these observations establish a positive correlation between KRAS*–driven invasiveness and lipid–rich CAF enrichment in human and murine CRC.

KRAS* upregulates proadipogenic cytokines to orchestrate lipo–fibrogenesis and promote tumor growth

The enrichment of lipid–rich CAFs in KRAS*–expressing tumor stroma prompted us to examine potential for KRAS* to regulate the expression of proadipogenic factors. As noted, lipo–fibrogenesis appears to co–opt the mechanisms driving classical adipogenesis. Specifically, the preadipocyte commitment phase of lipo–fibrogenesis and adipogenesis is driven by the inhibition of WNT signaling (46) and the activation of BMP signaling (47). PDGFRα$^+$ preadipocytes accumulate lipids via an FGF10 autocrine loop (48), and lipid droplet accumulation can be further promoted by insulin, cyclic amp, or glucocorticoids via PPARγ and C/EBPs upregulation (49).

As shown in Fig. 2A, the intersection of (i) differentially expressed genes in invasive iKAP versus non-invasive iAP, (ii) the human secretome, and (iii) the known pro- and anti-adipogenic secreted factors revealed KRAS*-regulated expression of 6 key BMP and WNT factors. Additionally, DOX modulation of KRAS* expression produced marked changes in the expression of well-established lipid–rich and proadipogenic regulatory factors and markers (Fig. S3A); and GSEA of stromal populations showed KRAS*–dependent enrichment of 2 major preadipocyte commitment drivers: RESPONSE_TO_BMP and NEGATIVE_REGULATION_OF_WNT (Fig. 2B and S3B). To validate these KRAS*-regulated proadipogenic cytokines, we measured their expression in KRAS*–on (+DOX) versus KRAS*–off (−DOX) primary 2–dimensional iKAP cancer cell cultures, revealing KRAS*-induced upregulation of BMP4 and WNT5B (Fig. 2C and S3C). BMP4 is known to induce the transformation of pluripotent stem cells into adipocytes via the SMAD and p38MAPK pathways (47); and WNT5B participates in noncanonical WNT signaling to inhibit β–catenin nuclear localization and also indirectly promotes the adipogenesis of progenitor cells (49). The KRAS*–WNT5B/BMP4 connection was confirmed in (i) 2 patient derived xenograft organoids (PDXOs) engineered with inducible KRAS activation (Fig. 2D upper panel) (ii) the murine CRC cell line CMT93 with and without KRAS*, (iii) iAP and iKAP tumor organoids, (iv) the human CRC cell line DLD1 isogenic for KRAS* and KRAS wild–type cell lines, and (v) the KRAS* and KRAS wild–type human CRC in TCGA dataset (Fig. S3D). Additionally, IHC staining confirmed increased BMP4 and WNT5B levels in KRAS*–expressing iKAP tumors compared with iAP controls (Fig. 2E). Wnt5b and Bmp4 expression levels positively correlate with tumor stages in the iKAP model but not in iAP model (Fig. 2F and S3E) indicating the KRAS* and stage dependency of Bmp/Wnt signaling in CRC development. This stage-dependency may relate to the subclonal nature of KRAS mutant cancer cells in early-stage disease (50), as well as changes in KRAS* downstream signaling as a function of tumor progression (51).

We next sought to validate the pro-adipogenic activity of KRAS*–regulated BMP4 and WNT5B in several model systems. First, the 3T3L1 cell culture model of adipocyte differentiation (52) confirmed that supplementation of insulin with recombinant BMP4/WNT5B increased adipocyte markers/regulators expression relative to insulin only controls (Fig. S3F). Second, undifferentiated 3T3L1 cell treatment with KRAS*–on, but not KRAS*-off, iKAP conditioned medium (CM) stimulated differentiation into adipocyte progenitor cells and lipid–rich fibroblasts (Fig. 2G and S3G), which expressed the adipocyte marker PPARG and lipid–rich fibroblast markers FGF10, TCF21 and PLIN4 (Fig. 2G, right). Third, using 2 patient derived xenograft organoids engineered with a DOX–inducible KRAS* allele and human CRC DLD1 cell line isogenic for KRAS* or wild–type KRAS showed that treatment of human mesenchymal stem cells (hMSCs) with KRAS* CM stimulated differentiation to adipocyte–like cells expressing lipid–rich fibroblast genes to a greater degree than did treatment with wild–type KRAS CM (Fig. 2H and S3H-I). Finally, we observed that lipo–fibrogenesis was increased specifically in collagen-expressing tumor stroma in tumors generated by the co-injection of 3T3L1 and KRAS*–on iKAP cancer cells and decreased in the tumors after 1–week KRAS* extinction by dox withdrawal (Fig. 2I and S3J).

In addition, Insulin pathway signaling is observed in iKAP bulk tumors and KRAS*-driven tumor stroma (Fig. S3K), indicating the presence of an active adipogenesis process within the KRAS* stroma. Together, these data support the view that KRAS* drives the expression of the pro-adipogenic cytokines WNT5B and BMP4 to promote stromal lipo–fibrogenesis.

These observations prompted us to investigate the potential biological impact of lipid–rich versus lipid–sparse CAFs on tumors. To that end, we isolated primary lipid–rich and lipid–sparse CAFs from iKAP tumors by flow sorting LipidTOX^{+}/PDGFRα^{+}/CD326^{-}/CD45^{-}/CD31^{-} and LipidTOX^{-}/PDGFRα^{-}/CD326^{-}/CD45^{-}/CD31^{-} cell populations for use in co–injection studies (Fig. 3A and 3B). The small population of lipid–sparse CAFs required brief expansion in vitro (See Methods “Lipid–sparse CAFs/myofibroblasts isolation”) and were subsequently validated for the expression of αSMA and RGS5 to confirm the CAF myofibroblastic cell type (Fig. S4A). Orthotopic co-injection of iKAP cancer cells and sorted, lipid–rich CAFs generated larger tumors (Fig. 3C) and reduced overall survival (Fig. 3D); immunofluorescence analysis of these tumors confirmed abundant lipid droplets in the tumor stroma (Fig. 3E). In contrast, orthotopic co-injection of iKAP cancer cells and lipid–sparse CAFs (myofibroblastic CAFs) generated tumors that grew more slowly and were associated with prolonged survival; immunofluorescence analysis revealed a paucity of lipid droplets in the tumor stroma and more prominent representation of αSMA^{+} cells (Fig. 3D-E). These findings are aligned with the above primary tumor single cell data, showing that αSMA^{+} CAFs are distinct from lipid–rich CAF subpopulations (Fig. 1F and S2A). Consistent with these murine studies, human CRC (TCGA) analyses established a positive correlation between advanced disease and increased lipid–rich CAF gene signatures (Supplementary Table S1: the combination of top 10 differentially expressed genes in 4 αSMA− CAF subgroups from mouse scRNA– seq; Supplementary Table S2: the combination of adipocyte and fibroblast genes (PanglaoDB)) (Fig. S4B) and a worse prognosis (Fig. 3F and S4C). Of note, myofibroblast gene signature (GSEA) and myofibroblast differentiation gene signature (GSEA) scores have no impact on CRC prognosis (Fig. S4D). Together, these results suggest that lipid–rich CAFs promote the progression of mouse and human CRC.

KRAS* regulates pro-adipogenesis cytokines through TFCP2

To determine how KRAS* drives pro-adipogenic cytokine gene expression, we surveyed transcription factor expression (53), transcription factor (TF) signatures, and consensus TF binding motifs present in the promotors of proadipogenic cytokine genes exhibiting KRAS*–dependent expression in murine and human CRC (Supplementary Table S3). Two TF candidates emerged from this data integration: sex–determining region Y (SRY, also known as testis–determining factor), which is responsible for the sex determination of males (54); and alpha–globin TFCP2 (Fig. 4A and S5A). We focused hereafter on TFCP2, given that it was the top candidate and that ERK1, a downstream effector of KRAS, is known to phosphorylate and increase TFCP2’s DNA binding activity (55). SRY was deprioritized because it is a Y chromosome gene expressed solely in males, yet our data indicated that KRAS* drives pro-adipogenic cytokine gene expression in both sexes.

To validate TFCP2's role in mediating KRAS*–driven, pro-adipogenic cytokine gene expression, TFCP2 was depleted (via short hairpin RNA) or deleted (via clustered regularly interspaced short palindromic repeats [CRISPR]) in iKAP cell lines. As an experimental control, we generated TFCP2–null clones that were rescued by re-expression of wild–type TFCP2. In the clones with TFCP2 depletion or deletion, WNT5B and BMP4 expression was decreased in the KRAS*–expressing cells yet restored in the TFCP2–rescued null controls (Fig. 4B and S5B). Chromatin immunoprecipitation (ChIP) using anti-TFCP2 antibodies confirmed the direct binding of TFCP2 to its consensus binding motifs in the WNT5B and BMP4 promotors (Fig. 4C and S5C-D). In addition, WNT5B and BMP4 reporter expression was decreased in the KRAS*–expressing TFCP2 depletion cells and restored by TFCP2–re-expressed rescue, validating the TFCP2 binding in WNT5B and BMP4 promotors (Fig. S5E). The role of TFCP2 in regulating the biology of CAFs and other cells of the tumor microenvironment was reinforced by the strong positive correlation between TFCP2–high gene signature scores and various stromal lineages, including endothelial cells, fibroblasts, and adipocyte signatures (43) (Fig. 4D). Functionally, the syngeneic and xenograft injections of iKAP TFCP2–depleted cancer cells generated smaller tumors that possessed fewer lipid–rich CAFs; whereas the lipid–rich CAFs were abundant in the TFCP2–rescued null controls (Fig. 4E-G and S5F). It is worth noting that TFCP2 depletion had no significant impact on cancer cell proliferation *in vitro* (Fig. S5G-H), suggesting that its prime actions may be exerted at the level of the tumor microenvironment.

TFCP2–high gene signature scores correlated positively with advanced invasive and metastatic disease and poor survival in patients with CRC (Fig. 4H, and S5I). This finding motivated us to determine the therapeutic impact of the TFCP2–specific small molecule inhibitor FQI1, which targets the TFCP2 DNA binding domain and eliminates downstream transcriptional activity (56). We first determined that FQI1 downregulated the canonical TFCP2–regulated genes *SPP1, MMP9*, and *CFH* (57) in cultured FQI1–treated iKAP cells (Fig. S5J). Next, we validated that FQI1 treatment of iKAP tumor cell lines decreased the expression of Wnt5b and BMP4 (Fig. 4I). In addition, FQI1 treatment of tumor–bearing iKAP mice reduced the accumulation of lipid–rich CAFs, and prolonged survival in autochthonous iKAP mice (Fig. 4J-K). Together, these findings provide strong evidence that KRAS*–dependent CRC progression is driven in part by the stimulation of lipo–fibrogenesis via the TFCP2–mediated regulation of proadipogenic cytokines.

Lipid–rich CAFs secrete VEGFA to promote tumor angiogenesis

To better understand the biological actions of lipid–rich CAFs in KRAS*–expressing CRC tumors, we surveyed murine and human CRC transcriptomic profiles for pathways and cell types enriched in tumors with high lipid–rich CAF gene signature scores. The top pathways were the ANGIOGENESIS and KRAS_SIGNALING_UP pathways. Per the cell type gene signature database, Panglao DB (43), the cell type occurrences associated with the highest lipid–rich CAF signature scores were fibroblasts, adipocytes, and endothelial cells (Fig. 5A, S6A). Notably, a heatmap analysis revealed that the endothelial cell signature was enriched in both the lipid–rich CAFs and KRAS*–driven invasive CRC tumors (Fig. 5B). These *in silico* data prompted us to hypothesize that a prime action of lipid–rich CAFs is to promote angiogenesis in the tumor microenvironment.

To identify the factors that may promote tumor angiogenesis in lipid–rich CAFs, we intersected several datasets and performed functional assays utilizing iKAP CM–educated 3T3L1 cells and KRAS*–expressing DLD1 CM–educated hMSCs. First, using adipokine array profiling, we determined that several secreted factors with known pivotal roles in tumor angiogenesis—including VEGFA, macrophage colony–stimulating factor, hepatocyte growth factor, lipocalin 2, pentraxin 3 (PTX3), and DLK1, a non–canonical ligand of Notch signaling—were upregulated in iKAP CM–educated 3T3L1 cells (Fig. 5C). Second, we performed a tumor scRNA–seq analysis, which confirmed increased VEGFA, pentraxin 3, and hepatocyte growth factor expression in the KRAS*–expressing iKAP tumor stroma compared with iAP and KRAS*–off (DOX–off) iKAP tumor controls (Fig. 5D and S6B). Correspondingly, reverse transcription polymerase chain reaction (RT–PCR) validated the significantly and consistently increased expression of VEGFA in DLD1 CM–educated hMSCs (Fig. 5E). Third, IHC and cytometry analysis confirmed the enrichment of VEGFA expression and the endothelial cell population ($CD326^{-}/CD45^{-}/CD31^{+}$) in KRAS*–expressing iKAP and KRAS*–expressing DLD1 tumors (Fig. 5F and S6C). The positive correlation between lipid–rich CAFs and VEGFA expression and endothelial cell counts in iKAP tumors aligned well with the results of our immunofluorescence analysis, which showed an enrichment of VEGFA and an increased number of $CD31^{+}$ endothelial cells in iKAP tumors and in tumors generated by the co-injection of iKAP cancer cells and $LipidTOX^{+}$–sorted cells (Fig. S6D). Finally, on the functional level, we assessed the proangiogenic activity of lipid–rich CAFs in human umbilical vein endothelial cell (HUVEC) tube–formation assays. The addition of CM from DLD1–$KRAS^{G12D}$ CM–educated hMSCs stimulated an increase in all conventional endothelial cell metrics, including the covered area, total tube length, total number of branching points, and total number of loops of the endothelial structure (Fig. 5G). Thus, lipid–rich CAFs promote tumor angiogenesis via the secretion of VEGFA.

Finally, the role of TFCP2 in mediating KRAS*–induced lipo–fibrogenesis and angiogenesis was solidified by demonstrating that TFCP2 depletion decreased VEGFA and endothelial cell density in KRAS*–expressing iKAP tumors compared with controls (Fig. 5H and S6E). In addition, inhibiting TFCP2 with FQI1 reduced VEGFA expression and the abundance of $CD326^{-}/CD45^{-}/CD31^{+}$ endothelial cells in KRAS*–expressing iKAP tumors (Fig. 5I). Analysis of the TCGA CRC dataset reinforced the TFCP2–VEGFA connection, as evidenced by the poor prognosis of CRC patients with high VEGFA expression, a TFCP2–high signature, or a combined VEGFA− and TFCP2–high signature (Fig. 4H and 5J). Correspondingly, treatment with FQl1 alone, the murine anti–VEGFA neutralizing antibody B20 alone, or both all impaired CRC progression in iKAP GEM (Fig. 5K). These survival curves uncover two noteworthy observations. First, treatment with FQl1 alone was equivalent to combination treatment with FQI1 and B20, consistent with VEGFA as a key downstream target for TFCP2. Second, FQI1 or FQI1+B20 treatments were more effective than B20 alone, suggesting that TFCP2 acts on additional targets beyond VEGF such as its additional angiogenesis targets as noted above (Fig. 5C). In contrast, FQI1 treatment of the iAP CRC model had no impact on improving survival relative to vehicle treated controls (Fig. S6F), reinforcing the specificity of TCP2 inhibition on angiogenesis to extend survival specifically in the context KRAS*. We conclude that KRAS*–activated TFCP2 promotes the

development of lipid–rich CAFs which contribute to the progression of CRC primarily via VEGFA–induced tumor angiogenesis. The preservation of the KRAS*–TFCP–VEGFA axis in human KRAS*–driven CRC portends its translational potential of clinical research and further raises the possibility that targeting TFCP2 may prove more effective than VEFGA neutralization in CRC.

DISCUSSION

In this study, exploration of the mechanisms governing KRAS*–mediated CRC progression revealed its role in activating TFCP2–induced transcriptional upregulation of proadipogenic cytokines in cancer cells, which in turn stimulates the lipogenic transformation of CAFs in the tumor microenvironment. These lipid–rich CAFs produce abundant VEGFA to promote tumor angiogenesis and disease progression. We found that the genetic or pharmacological neutralization of TFCP2 impeded CAF adipogenesis, reduced tumor angiogenesis, and inhibited tumor growth in mouse and human KRAS*–expressing CRC models. In CRC, KRAS* is known to regulate numerous hallmarks, including those intrinsic to cancer cells and those regulating the tumor immune microenvironment. This study now expands the known actions of KRAS* to the phenotypic transformation of CAFs with enhanced pro–tumorigenic properties. Our findings also indicate that the KRAS*–TFCP2–VEGFA axis provides a testable therapeutic option for KRAS*–driven CRC patients.

The lipid–laden CAF cells identified in this study are reminiscent of the lipid interstitial cells present in the developing murine lung (58, 59) and cells in adipogenesis (49). First, analogous to the lipid–rich CAF–endothelial cell heterotypic interactions, lung lipofibroblasts provide a nurturing environment for stem cell growth (60, 61) by enhancing oxidative defenses, providing leptin to stimulate surfactant synthesis in type 2 alveolar epithelial cells, and promoting type 2 cell proliferation (62). Second, additional parallels between lipid–rich CAFs and alveolar lipofibroblasts are seen in lineage–tracing analyses. These analyses show that PDGFRα$^+$ progenitor stromal cells differentiate into alveolar lipofibroblasts (63), which contain an abundance of neutral lipids; lipid droplet–associated protein (perilipin); the adipocyte markers TCF21, FABP4, LPL, and ZFP423; membrane–tethered COL13A1; and FGF10 (29-31). Similarly, lipid–rich CAFs and alveolar lipofibroblasts share a similar gene expression profile that includes LPL, perilipin, TCF21, FGF10, PI16, CLO12A, and MMP13 (Fig. 1D and S1D-E). Third, in both lipofibrogenesis and adipogenesis, FGF10 has been implicated in the transformation of PDGFRα$^+$ preadipocytes into beige adipocytes via a miRNA–327–FGF10–FGFR2 autocrine loop (48). Similarly, KRAS* CM induced the expression of FGF10 which educated and transformed embryonic fibroblast and mesenchymal stem cells into lipid–rich fibroblasts in cell culture (Fig. 2G, 2H and S3I). KRAS* functioned similarly in the iKAP tumor microenvironment (Fig. S2F). Among the similarities between lipid–rich CAFs and adipocytes is their emergence from a common progenitor cell, the PDGFRα$^+$ preadipocyte (48). In adipogenesis, the inhibition of canonical WNTs and the activation of BMP signaling facilitates the commitment of preadipocytes towards an adipogenic fate; and insulin stimulates adipocyte maturation with lipid droplet accumulation. Correspondingly, iKAP cell lines exhibit KRAS*–dependent enrichment of the 2 main proadipogenic cytokines, the key molecules BMP4 and WNT5B (Fig. 2C and S3C); iKAP bulk tumors and

KRAS*-driven tumor stroma exhibit insulin pathway signaling (Fig. S3K) consistent with an active adipogenesis process in KRAS* stroma. Together, these findings establish that lipid–rich CAFs co–opt the mechanisms governing normal lipofibrogenesis and adipogenesis programs.

Our focus on angiogenesis relates first and foremost to tumor histopathological analyses showing that KRAS* is associated with increased tumor angiogenesis. Second, an unbiased GSEA analysis of KRAS*–regulated pathways that are shared and enriched in both mouse and human KRAS* CRC showed a strong and prominent correlation between EMT and angiogenesis pathways and the lipid–rich CAF gene signature. Third, cytokine array screens of the CAF secreted factors show the secretion of VEGFA, MCSF, DLK1, HGF and LCN2 in KRAS*–conditioned medium cultured–embryonic fibroblasts (lipid–rich CAFs). Together, these data support our prioritization of angiogenesis as a major cancer hallmark regulated by lipid–rich CAFs. More generally, this prioritization is justified on several levels by evidence supporting angiogenesis as a driver of tumor progression including (i) increased VEGFA expression correlating negatively with overall survival in TCGA (Fig 5J), (ii) higher CD31 staining in invasive iKAP tumors relative to non–invasive iAP tumors (Fig. 5F), and (iii) the clinical benefit of anti–VEGFA mAb in iKAP model (Fig. 5K). Thus, we are confident that angiogenesis is a very important aspect of the tumor biological impact of lipid–rich fibroblasts in KRAS* CRC, although we acknowledge that we cannot exclude the possibility lipid rich–CAFs modulates addition cancer hallmarks that contribute to tumor progression such as EMT (Fig. 5A).

With respect to the mechanism of VEGF upregulation in lipid-rich CAFs, we speculate that prostaglandin E2 (PGE2) is the upstream metabolite driving VEGFA expression specifically in lipid-rich CAFs. Lipid droplets are known to be the major reservoirs of diverse metabolites including PGE2 (64). Our expression data show that the key PGE2 synthesis enzymes and PGE2 receptors are indeed enriched in the lipid-rich CAFs, but not in the myofibroblasts (Fig. S6G). Moreover, PGE2 ELISA analysis shows that PGE2 is enriched in the iKAP tumors relative to iAP tumors and in the conditioned media from KRAS–on iKAP fibroblasts (lipid-rich fibroblasts) (Fig. S6H-I). PGE2 has been shown to bind its receptor PTGER to activate downstream ERK/JNK signaling which can upregulate VEGFA expression (65) – accordingly, PTGER1 and 4 are expressed in lipid-rich CAFs (Fig. S6G lower panel) and depletion of the key PGE2 synthesis enzyme PTGS2 in the KRAS–on conditioned media-educated 3T3L1 cells results in decreased VEGFA expression (Fig. S6J). Thus, the lipid-rich CAF-derived PGE2 can upregulate VEGF upregulation via a paracrine, autocrine and/or intracrine manner as proposed by (66) and operates similarly in our model system.

Our work identifies TFCP2 as a key downstream target of KRAS* in driving the proangiogenic adipogenic program. TFCP2 regulates MMP9 expression, which promotes angiogenesis in hepatocellular carcinoma (HCC) (57). TFCP2 binds to YAP as a cofactor to regulate gene transcription, including MMP9, FN1, and TJP1 and contributes to YAP–dependent liver malignancy (67). In CRC, however, there remained a more limited understanding of TFCP2's actions. Previous work has shown that TFCP2 binds to CPEB1's hypermethylated TF–binding region to suppress the expression of CPEB1 and promote

tumor metastasis (68). In our CRC studies, TFCP2 acted in an entirely different manner by directly upregulating WNT5B and BMP4 gene transcription to spur the development of VEGFA–expressing, lipid–rich CAFs (Fig. 4C and 4F). In addition, although TFCP2 regulates MMP9 expression in HCC, this was not observed in the CRC model, likely because MMP9 is mostly expressed in myeloid cells and has low or no expression in cancer cells. Moreover, TFCP2–driven lipid–rich CAF is the major source of VEGFA (another source being myeloid cells), indicating their important contribution in tumor angiogenesis. Given that a high–TFCP2 signature is associated with a worse prognosis in patients with CRC (Fig. 4H), it is encouraging that, in our preclinical models, FQ1's inhibition of TFCP2 was well tolerated and impaired lipofibrogenesis, tumor angiogenesis, and tumor progression (Fig. 4J, 4K, 5I and 5K). FQI1 has been shown to impair tumor growth in subcutaneous xenograft and spontaneous Alb–cMyc HCC models (56, 69), pointing to the need for additional investigations of the role of TFCP2 in other tumor types and genotypes. In CRC, our findings rationalize the testing of adjuvant FQI1 treatment in early–stage KRAS*–driven CRC patients at high risk for metastases, i.e., Stage II patients with large amounts of circulating tumor DNA after surgery. Moreover, the lipid–rich CAF/TFCP2–high signature may serve as a patient–selection biomarker to enlist CRC patients into such targeted TFCP2 trials designed to reduce disease recurrence. Current therapies targeting KRAS* in cancers show promise, but resistance to KRAS* inhibitor therapies is occurring in human trials, underscoring the need to define the spectrum of targetable biological actions of KRAS* in CRC.

METHODS

Cell culture

iKAP primary cell line cultures were sorted from GFP^+, iKAP–dissociated tumors and cultured in Dulbecco Modified Eagle's Medium (Gibco; 11995-065) with or without DOX supplementation (2 μg/mL). CMT93 (ATCC; CCL–223), 293T (ATCC; CRL–3216), and 3T3L1 (ATCC; CL–173) cell lines were cultured in DMEM, supplemented as defined by ATCC. DLD1 isogenic KRAS wild–type CRC cells were cultured in RPMI–1640 medium (Gibco; 11875-093). hMSC (ATCC ; SCRC–4000) was obtained from ATCC and cultured in Mesenchymal Stem Cell Basal Medium (ATCC PCS-500-030), supplemented as defined by ATCC. HUVEC (CRL–1730) as obtained from ATCC and cultured in F-12K Medium (ATCC; 30-2004), supplemented as defined by ATCC. All cell lines were cultured in the indicated medium containing 10% fetal bovine serum or bovine calf serum (Sigma) and an 1% Antibiotic–Antimycotic (Gibco; 15-240-062) following ATCC's instructions. All cells were confirmed to be mycoplasma–free using Mycoplasma Elimination Kit (Sigma; MP0030) and maintained at 37 °C and 5% CO_2.

For supplemental recombinant Bmp4 and Wnt5b proteins used for adipogenic cell differentiation, 100 ng/mL Bmp4 (R&D; 5020–BP–010) and 100 ng/mL Wnt5b (R&D; 3006–WN–025) were added to complete 3T3L1 medium. After 2 weeks, the medium was supplemented with 10 μg/mL insulin for 2 days. The transcription expression of adipogenic genes was validated using RT–qPCR.

Conditioned media (CM) was collected from iKAP cell lines, DLD1 cell lines, and PDXOs after culturing for 24 hours in complete culture medium as specified for each experiment. Following a published protocol (70), In vitro differentiation was achieved by co-culturing 3T3L1 cells or hMSCs with the iKAP CM or DLD1 cell lines' CM for 16 days. Old CM was exchanged for fresh CM every 2 days. In the last 2 days, adipogenic terminal differentiation was initiated by adding insulin to 10 μg/mL (Sigma; 11070–73-8, and Sigma; 11061-68-0), 3–isobutyl–1–methylxanthine 500 μM (Sigma; I7018), and dexamethasone 700 nM (Sigma; D4902). Immunoblotting, RT–qPCR, IHC, and immunofluorescence procedures were performed to validate adipogenic differentiation by confirming the presence of adipocyte and lipid-rich fibroblast related genes.

Patient derived xenograft organoids establishment and maintenance

Human studies followed Helsinki Declaration ethical guidelines and were conducted under an Institutional Review Board-approved protocol at MD Anderson Cancer Center. All patients provided written, informed consent for tissue distribution and specimen collection. To generate organoids, primary human tumor xenografts were minced and digested in digestion buffer (DMEM (Gibco; 11995-065) plus 100 U/ml Penicillin/Streptomycin (Gibco; 15140-122), 500 U/ml Collagenase IV (Thermo; 17104019), and 125 mg/ml Dispase type II (Thermo; 17105041)) for 30 minutes at 37 °C. The samples were washed with DMEM/5% FBS and PBS sequentially, and the digested tumor cells were resuspended in Matrigel and plated onto a 24–well culture plate (approximately 10 % confluent in 30 mL droplet per well). After the gel solidified, 500 ul of WENR medium (Advanced DMEM/F12 medium (Gibco; 12634-010) plus 1 mM GlutaMAX (Gibco; 35050-061), 1 mM HEPES (Gibco; 15630-080), and 100 U/ml Penicillin/Streptomycin (Gibco; 15140-122), supplemented with 50% Wnt–3A conditioned medium from L-Wnt3A cells (ATCC; CRL-2647), 10% R–spondrin–1 conditioned medium from Rspondrin1 cells (Sigma; SCC111), 100 ng/ml hNoggin (R&D; 6507-NG), 10 nM hGastrin I (Sigma; G-9145), 500 nM A83–01 (Tocris; 2939), 10 uM SB202190 (Sigma; S7067), 10 mM Nicotinamide (Sigma; N0636), 1X B27 supplement (Gibco; 008-0085SA), 1X N2 supplement (Gibco; 17502-048), 1 mM N–acetyl cysteine (Sigma; A9165), and 50 ng/ml hEGF (R&D; 236-EG)) was added to wells and incubated at 37 °C.

Established organoids were routinely passaged every 10 to 14 days, at a cell density of approximately 50 % confluent. Organoids were released from Matrigel by incubating with Cell Recovery Solution (Corning; 354253) at 4 °C for 30-40 minutes. Released organoids were broken down into small fragments by physical pipetting, or further dissociated with TrypLE Express Solution (Gibco; 12604013) at 37 °C for 3-5 minutes to obtain smaller fragments or homogeneous single cells. After washing with PBS, the resulting fragments and cells were resuspended with Matrigel (Corning; 356231) and plated onto a 24–well culture plates (Thermo; 142475) with a typical split ratio = 1:3–1:4. Culture medium was refreshed every 2 to 3 days. For quality control, the organoid cultures were regularly checked STR sequencing for mycoplasma. For long–term storage, organoid fragments or dissociated single cells were resuspended in cold Recovery Cell Culture Freezing Medium (Gibco; 12648010), gradually frozen down to −80 °, and stored in liquid nitrogen.

Tumor models and treatments

The iKAP CRC mouse model (Villin–Cre–ERT;Apclox/lox;Trp53lox/lox;tet–O–LSL–$Kras^{G12D}$) and iAP mouse model (Villin–Cre–ERT;Apclox/lox;Trp53lox/lox) were previously established and the histopathological identification of invasive and noninvasive tumors in the models were previously validated as described (7). Mouse colony management and tumor observations under colonoscopy were conducted as previously described (7). To induce colorectal tumors in iKAP and iAP mice, 20 μl of 4–OHT (1 mg/mL) in 100% ethanol was injected directly into the distal colon lumen followed by DOX water feeding (200 mg/kg) at 10 to 16 weeks of age. Treatment as described here was initiated after mice had received 1 4–OHT injection and 14 days of DOX water. 4-OHT injected iKAP mice (equal numbers of males and females) were randomly assigned to receive FQI1 or VEGFA mouse antibody (B20) treatment. FQI1 (1 mg/kg) or vehicle (phosphate–buffered saline + 0.4% DMSO) were given 5 days a week; B20 (10 mg/kg) or IgG isotype control (10 mg/kg) were given 3 times a week by intraperitoneal injection. Mice were sacrificed when they became moribund, and their tumors were collected.

All surgical manipulations were performed under isoflurane anesthesia, and all animal experiments were approved by The University of Texas MD Anderson Cancer Center's Institutional Animal Care and Use Committee. For the orthotopic xenograft co-injection model, 10^5 iKAP cells and 10^4 fluorescence–activated cell–sorted, lipid–rich or lipid–scarce fibroblasts in growth factor–reduced Matrigel were co-injected into the cecum wall of the mice. Mice were monitored for survival and sacrificed when moribund. A set of mice was sacrificed 4 weeks after injection to measure tumor volumes. For the syngeneic transplantation and xenograft tumor models, 10^5 Tfcp2–engineered iKAP cells were suspended in growth factor–reduced Matrigel and injected subcutaneously. Syngeneic transplanted tumors were collected at 4 months and xenograft tumors were collected at 1.5 months.

Plasmids, viral transfections, and cloning

Four mTfcp2 knockout guide RNAs were designed in CHOPCHOP (71) and were screened for their efficacy in reducing messenger RNA (mRNA) and protein levels by at least 80%. The guide RNA sequences 5'– GACGACGTGATCCAAATCTGCGG–3' and 5'–GCCTGTCGTGGAACACTACGCGG–3' were inserted into LentiCRISPR v2 plasmids following the standard protocol (72). LentiCRISPR v2 was a gift from Feng Zhang (Addgene plasmid # 52961, http://n2t.net/addgene:52961; RRID, Addgene_52961). Serial dilution of each mTfcp2 knockout clone in a 96–well plate produced colonies from single cells. After testing the knockout efficacy of Tfcp2 in each colony, 2 single clones from 2 guide RNAs knockout cells were designated as cell lines Tfcp2–KO1 and Tfcp2–KO2. Four short hairpin RNAs targeting mTfcp2 in the pLKO.1 vector (Sigma) were screened and chosen for their efficacy of reducing mRNA and protein levels by at least 80%. The TRCN0000218063, TRCN0000085495, and TRCN0000225944 clones (Sigma) were selected for further use. mTfcp2 overexpression plasmids were purchased from GenScript (NM_033476.3; cloning mTfcp2 protein coding sequence into pInducer20 vector, mTfcp2–DYK_pInducer20). Lentiviral particles (8 μg) were generated by transfecting 293T cells with the packaging vectors psPAX2 (4 μg) and pMD2.G (2 μg). Lentiviral particles in

medium were collected 48 and 72 hours after the transfection of 293T cells, and the medium was filtered through a 0.45–μm filter (Corning; 430514). Viral medium was used in a 1/3 dilution of complete medium for cell culture. After 24 hours, fresh DMEM was provided. At 48 hours, cells were selected following 72 h of treatment with Puromycin (2 μg/mL). Cell lines were then cultured in complete medium.

Immunoblotting

Immunoblotting was performed following standard protocol (the R&D Systems Quality Control Western Blot Protocol). Antibodies, including β–actin (Sigma, #A3854), vinculin (Millipore 05–386), Bmp4 (Abcam, ab124715), Bmp2 (Abcam, ab82511), Wnt5a (Abcam, ab229200), Wnt5b (Abcam, ab94914), Wnt10b (Abcam, ab70816), insulin (Abcam, ab181547), $KRAS^{G12D}$ (Cell Signaling, 14429S), and Tfcp2 (Cell Signaling, 80784S), were purchased. Quantifications were performed using Image J software, and the results were normalized using the first control band.

IHC and immunofluorescence

Invasive iKAP, non-invasive iAP, and non-invasive iKAP–DOXoff (KRAS*–off) CRC tumors were collected from micro–dissected localized adenomas and invasive adenocarcinomas. These tumors were analyzed by IHC and immunofluorescence as describe below.

IHC was performed following R&D Systems' Protocol for the Preparation and Chromogenic IHC Staining of Frozen Tissue Sections and Protocol for the Preparation and Chromogenic IHC Staining of Paraffin–embedded Tissue Sections. Lipid droplet staining by oil red and/or LipidTOX were performed on frozen tissue sections. Antibody staining was done on paraffin–embedded tissue sections after antigen retrieval using a pressure cooker (95 °C for 30 min followed by 120 °C for 10 s) and incubation in antigen–unmasking solution (Vector Laboratories). For frozen tissue sections, antibody and lipid droplet staining was performed after 4% formalin fixation. Oil Red O Stain Kit (Lipid Stain; ab150678) was used for lipid droplet staining. The antibodies used included Pdgfrα (Cell Signaling, #3174), Lpl (Invitrogen, PA585126), $KRAS^{G12D}$ (Cell Signaling, 14429S), Thy1 (eBioscience, 14–0900–81), Col3a1 (proteintech, 22734–1–AP), Fabp4 (Abcam, ab92501), Dlk1 (Abcam, ab119930), Tcf21 (Invitrogen, PA5116012), Vegfa (Invitrogen, MA5–32038), and Cd31 (Invitrogen, PA5–16301). Slides were scanned using a Pannoramic 250 Flash III scanner (3DHISTECH Ltd), and images were captured using Pannoramic Viewer software (3DHISTECH Ltd). IHC quantification was conducted following bio–protocol (73) to measure 3,3'–diaminobenzidine staining and quantify the average pixel intensity. Immunofluorescence was performed using the Protocol for the Preparation and Fluorescent IHC Staining of Frozen Tissue Sections (R&D Systems). Purchased lipid–staining dyes included HCS LipidTOX Deep Red Neutral Lipid Stain (Invitrogen, H34477) and HCS LipidTOX Red Neutral Lipid Stain (Invitrogen, H34476). Antibodies included those specific for αSMA (Abcam, ab124964), Cd326 (eBioscience, 11–5791–82), Dlk1 (Abcam, ab119930), Fabp4 (Abcam, ab92501), Col3a1 (proteintech, 22734–1–AP), Lpl (Millipore, MABS1270), Pdgfrα (Cell Signaling, #3174), and Cd31 (Invitrogen, PA5–16301). Images

were captured using a fluorescence microscope (Leica DMi8). Quantification was performed using Fuji (74) and Image J (75).

Flow cytometry and sorting

iKAP and iAP tumors were dissociated following the protocol, Dissociation of Single Cell Suspensions from Human Breast Tissues at protocols.io (http://dx.doi.org/10.17504/protocols.io.t3aeqie). Dissociated primary cells were stained with antibodies and/or dyes, including Cd326 (eBioscience, 11–5791–82), Cd45 (Biolegend, 103137), Cd31 (Biolegend, 102427), CD140a (Biolegend, 135906), and LipidTOX Deep Red Neutral Lipid Stain (Invitrogen, H34477). After being washing twice using cold phosphate–buffered saline, lipid–rich CAFs and endothelial cells were analyzed using a flow cytometer (BD LSRFortessa™ X–20 Cell Analyzer) or were flow–sorted using a BD FACSAria Flow Cytometer.

Lipid–sparse CAFs/myofibroblasts isolation

Lipid–sparse CAFs were collected by gating on CD326−, CD45−, CD31−, PDGFRα−, and LipidTOX^{low}. The lipid–sparse CAFs were cultured in a 2D culture dish to expand myofibroblasts and exclude pericytes following the JoVE and MIMB protocols (76, 77). Briefly, the selection was conducting by culturing cells in RPMI 1640 medium (Gibco; 11875-093) with 10% FCS, 50 μM 2-mercaptoethanol (Sigma; M6250-10ML), 100 μM asparagine (Sigma; PHR2350), 2 mM glutamine (Sigma; 1294808) and 1% Antibiotic–Antimycotic (Gibco; 15-240-062) in 2D culture dish (Corning; 430167). Pericyte grows on Pericyte growth medium (Pericyte Growth Supplement (ScienCell 1252, San Diego, CA) in Pericyte Medium (ScienCell 1201)) and grows on Collagen I coated plate. After expanding the myofibroblasts for 4 subculturing, cells were validated by measuring ACTA2, RGS5, and PDGFRα expression levels by RT–qPCR and immunofluorescence staining. The validated myofibroblasts were used for in vivo tumor co–injection assay.

ChIP–qPCR and Luciferase Reporter Assay

ChIP–qPCR was performed using the standard protocol described previously (78). Briefly, iKAP cells were crosslinked for 10 minutes using 1% paraformaldehyde, then reactions were quenched for 5 minutes using glycine at room temperature. Cells were lysed for 30 minutes with ChIP lysis buffer (78) on ice. Chromatin fragmentation was performed using a Diagenode BioruptorPico sonicator (45 cycles, each with 30 sec on and 30 sec off). Solubilized chromatin was then incubated with a mixture of Tfcp2 antibody (Cell Signaling, 80784S) in 1:100 dilution and Dynabeads (Life Technologies) 4°C overnight. Immune complexes were then washed 3 times with RIPA buffer, then once with RIPA–500, and once with LiCl wash buffer. Elution and reverse crosslinking were performed overnight at 65 °C in a direct elution buffer containing proteinase K (20 mg/mL). Eluted DNA was purified using AMPure beads (Beckman–Coulter) and was then used to perform qPCR. Three Bmp4 and Wnt5b primer pairs each were used (listed in Supplementary Table S4).

For luciferase reporter assay, the promoter region of human *BMP4* and *WNT5B* (−1500 to +500 bp) was amplified by PCR and inserted into the pGL3 vector (Addgene: E1751) to generate the corresponding reporter constructs. The luciferase reporter assay was conducted

by transfecting the reporter constructs and *Renilla* luciferase vector into iKAP TFCP2 knockout and rescued cell lines. Cells were harvested after 24 hours of transfection and luciferase activity was measured.

PGE2 ELISA

PGE2 analysis was performed using the Prostaglandin E2 ELISA Kit following the manufacturer's protocol (Abcam, ab133021). Briefly tumors were homogenized and centrifuged to collect the supernatant to measure the amount of PGE2. Additionally, conditioned media from iKAP–DOXon and –DOXoff CM–cultured 3T3L1 cells were collected to measure PGE2 levels.

Adipokine array

An adipokine array was performed using the Proteome Profiler Mouse Adipokine Array Kit following the manufacturer's protocol (R&D Systems; ARY013). Briefly, cell lysates were diluted, mixed with a cocktail of biotinylated detection antibodies, and incubated with a Proteome Profiler Mouse Adipokine Array. Control antibodies from the kit were used as the reference spots on the upper left corner of the arrays.

Angiogenesis assay

Human umbilical vein endothelial cell (HUVEC) tube–formation assay was performed using CM from lipid–rich CAFs. CM from DLD1–KRAS^{G12D} CM–educated hMSCs was cultured with HUVEC cells on Matrigel (Corning, 47743–722), and a web–based Wimasis Image Analysis tool (https://www.wimasis.com/en/) was used to analyze tube formation, including the covered area (%), total tube length (px), total branching points, and total loops.

Real–time quantitative PCR (RT–qPCR)

Cell pellets from iKAP cell line, sorted lipid–rich fibroblasts, CM–cultured 3T3L1 and hMSCs, and FQI1 treated iKAP cell lines were collected, and isolated mRNA was recovered using an RNeasy Mini Kit (Qiagen). mRNA was reverse–transcribed into copy DNA using a OneScript Plus cDNA Synthesis Kit (ABM; G236). SYBR Green PCR Master Mix (Thermo Fisher Scientific) was used to perform RT–qPCR in a 7500 Fast Real–Time PCR Machine (Applied Biosystems). The genes were normalized using actin and/or Ywhaz, an adipocyte internal control gene (79). qRT–PCR primers are listed in Supplementary Table S4.

RNA sequencing and analysis

Before performing RNA sequencing, iKAP and iAP tumors were assessed for KRAS* expression by IHC, as well as by IF and IHC of GFP, which is expressed by enema OHT/Cre-induced reporter activation. The tumor stages were verified by a GI pathologist, blinded to the sample identities. The tissues for RNA isolation were collected from micro-dissected localized adenomas and invasive adenocarcinomas (T4).

The RNA sequencing of CRC GEM tumors was performed as described in Boutin et al. 2017 (7), and the data were deposited in the National Center for Biotechnology Information under SRA number SRP097890. Briefly, cells were first lysed with Buffer RLT and then purified with TRIzol Reagent (Life Technologies) and chloroform. The remaining steps

of the RNeasy Mini Kit were then followed. RNA sequencing libraries were made, and samples were run on an Illumina HiSeq 2000 at The University of Texas MD Anderson Cancer Center Sequencing and Microarray Core Facility. Transcriptome reads were mapped to the reference mouse genome mm10, normalized, and quantified as fragments per kilobase per million mapped fragments values using HTSeq–count. A differential gene expression analysis was performed based on the results of the negative binomial distribution. Genes were compared for iAP vs. iKAP; iKAP vs. iKAP DOX–off; high vs. low lipid–rich CAF scores; and high vs. low Tfcp2 scores). The lipid–rich CAF gene signatures are listed in Supplementary Tables S1 and S2. The TFCP2− and SRY–regulated gene signatures were obtained from GSEA datasets (C3 TFT). The results from the comparisons were subjected to GSEA and heatmap analyses.

Single cell RNA sequencing and analysis of mouse and human CRC

Three independent samples each of invasive iKAP, non-invasive iAP, and non-invasive iKAP–DOXoff (KRAS*–off) CRC tumors were collected from micro–dissected localized adenomas and invasive adenocarcinomas. These tumors were freshy harvested for tumor dissociation and single cell sequencing analyses. Tumors were collected 2 months after TAM/DOX tumor induction and approximately 1 cm^3. For the iKAP–DOXoff (KRAS*–off) CRC tumors, doxycycline was discontinued for 7 days following 7 weeks of TAM/DOX tumor induction. scRNA sequencing was performed by MD Anderson's CPRIT Single Core. Single–cell capture, barcoding and library preparation were performed by following the Single–Cell Chromium 3′ protocol (10X Genomics; PN–120237) using V3 chemistry reagents (10X Genomics). The final libraries containing barcoded single–cell transcriptomes were sequenced at 100 cycles on an S2 flowcell on the Novoseq 6000 system (Illumina). Data were processed using the CASAVA 1.8.1 pipeline (Illumina), and sequence reads were converted to FASTQ files and UMI read counts using the CellRanger software (10X Genomics). For in–silico analyses, raw count matrices were converted to Seurat objects for further analysis. The quality of scRNA–seq data was measured by the percentage of mitochondrial genes (percent.mt) per cell and the number of unique molecular identifiers (UMI count). Low–quality cells with a UMI count less than 800, a percent.mt greater than 25%, and doublets expressing both cell type markers were removed. The batch effect was counteracted using the reciprocal PCA–based integration method in Seurat. We then performed unsupervised dimension reduction and clustering for cell identification. The annotation of cell identities in each cluster was based on both the canonical marker genes and the cluster differential genes. For module score plots, we perform Seurat's AddModuleScore using adipocyte gene signature (43), and the combination of classic adipocyte and pre-adipocyte genes (mature adipocyte markers: Fabp4, Lpl, Plin4, Dcn, Dpt, Cfd, Ccl2; mature adipocyte regulatory TFs: Pparg, Cebpa, Cebpb; pre-adipocyte markers: Dlk1, Dlk2, Lpl, Plin4; pre-adipocyte regulatory TFs: Zfp423, Tcf21) (29-31, 44, 45). All GEM CRC scRNA sequencing data were deposited in the National Center for Biotechnology Information (GSE229559); R code and R processed data were deposited in Code Ocean https://codeocean.com/capsule/1830109/.

Human research was conducted in accordance with the Helsinki Declaration ethical guidelines. Human tumor specimens were collected at The University of Texas MD

Anderson Cancer Center under Institutional Review Board approved protocol LAB10-0982 (PI: Dr Scott Kopetz) after obtaining written informed consent from each participant. Fresh specimens were shortly transported to MD Anderson's CPRIT Single Core in sterile cold DMEM medium for single cell isolation, scRNA sequencing, and analyses as described above. Clinical information, including tumor location, gender, age, stage at collection, MS status and genotype are listed in Supplementary Table S5. The raw single-cell RNA sequencing and processed data generated from human CRC specimens are available on Gene Expression Omnibus under accession number GSE231559.

Computational analysis of TCGA–COAD data

For human CRC data analyses, gene expression and survival data were obtained from TCGA–COAD datasets and/or datasets from cBioPortal (https://www.cbioportal.org/). We collected data including tumor genotypes, patient survival, tumor stages, tumor subtypes, and patient treatments in cBioPortal. Using R packages (DESeq2, GSVA, and pathfindR), we analyzed the enriched pathways in KRAS* patients, the KRAS-related genes, lipid–rich CAF scores, TFCP2 scores, and their roles in patient survival. Briefly, for pathway analyses, we obtain differential expression genes in KRAS* patients by DESeq2 and performed GSEA analyses or used pathfindR to obtain enriched pathways. For lipid–rich CAF scores and TFCP2 scores, we perform GSVA using lipid–rich CAF gene signature (Supplementary Table S1 and S2) and TFCP2 regulated gene signature (GSEA datasets, C3 TFT) from KRAS* and $KRAS^{WT}$ patients.

The analysis of KRAS* downstream TFs

The candidates of KRAS* downstream TFs were analyzed by utilizing the consensus TF binding motifs present in the promoters of BMP4 and WNT5B (PROMO software), along with the transcription factor (TF) signatures modulated in a KRAS*-dependent manner in both murine and human CRCs (GSEA analyses). The candidate lists from these three gene sets are listed in Supplementary Table S3.

Statistical analysis

All two–sample statistical analyses were performed using Student's t test, two sided, and were represented as the mean ± the standard deviation (SD). The significance analysis of the TCGA colon adenocarcinoma database, GEM RNAseq, scRNAseq, RT–qPCR, IHC quantification, and angiogenesis assay quantification were all performed in EXCEL and GraphPad Prism 9. Analyses of survival data from the TCGA colon adenocarcinoma database and GEM mice were performed using the Log–rank (Mantel–Cox) test in GraphPad Prism 9. *P* values are included in the graphs. *P* value <0.05 was considered statistically significant.

Data Reproducibility and Availability

Additional images for all tissue staining are provided in Fig. S7A-T; The RNA sequencing data of CRC GEM tumors were deposited in the National Center for Biotechnology Information under SRA number SRP097890; the GEM CRC scRNA sequencing data generated in this study are publicly available in Gene Expression Omnibus (GEO)

at GSE229559; R code and R processed data were deposited in Code Ocean https://codeocean.com/capsule/1830109/; the human CRC scRNA sequencing data generated in this study are publicly available in Gene Expression Omnibus under accession number GSE231559.

Supplementary Material

Refer to Web version on PubMed Central for supplementary material.

ACKNOWLEDGMENTS

The authors thank Dr. Douglas Hanahan and Dr. Krisztian Homicsko (the Swiss Federal Institute of Technology Lausanne) for invaluable feedback on our manuscript and for providing anti-mouse VEGFA mAb (B20); Dr. Bert Vogelstein (Johns Hopkins) and Dr. Jihye Yun (Baylor College of Medicine) for providing KRAS wild type DLD1 isogenic CRC cell lines; Dr. Nicholas Navin (The University of Texas MD Anderson Cancer Center) for performing single cell sequencing and analysis; Dr. Guillermina Lozano, Dr. Filippo G. Giancotti, and Dr. Traver Hart (MD Anderson Cancer Center) for providing manuscript and data analysis consultations; Dr. Kuo-Shun Hsu and Vincent Li (MD Anderson's TRACTION) for Patient derived xenograft organoids establishment and maintenance; Laura L. Russell, scientific editor (Research Medical Library at MD Anderson Cancer Center) for editing this article.

Financial support:

This work was supported by MD Anderson Cancer Center's Cancer Prevention & Research Institute of Texas (CPRIT) Single Cell Genomics User Group grant (RP180684), a CPRIT Research Training Program grant (RP210028; W.H.H. and K.A.L.), a National Institutes of Health (NIH) F99/K00 grant (CA274661–01; W.H.H.), MD Anderson Cancer Center UTHealth Graduate School of Biomedical Sciences' Pauline Altman–Goldstein Foundation Discovery Fellowship (W.H.H), an NIH R01 grant (CA231360; R.A.D.), National Center for Advancing Translational Sciences awards (TL1TR003169 and UL1TR003167; K.A.L.), the American Legion Auxiliary Fellowship in Cancer Research (K.A.L.), the Dr. John J. Kopchick Fellowship (K.A.L.).

REFERENCES

1. Li J, Ma X, Chakravarti D, Shalapour S, and DePinho RA (2021). Genetic And Biological Hallmarks Of Colorectal Cancer. Genes Dev 35, 787–820. 10.1101/gad.348226.120. [PubMed: 34074695]
2. Siegel RL, Miller KD, Fuchs HE, and Jemal A (2022). Cancer Statistics, 2022. CA Cancer J Clin 72, 7–33. 10.3322/caac.21708. [PubMed: 35020204]
3. Manfredi S, Lepage C, Hatem C, Coatmeur O, Faivre J, and Bouvier AM (2006). Epidemiology And Management Of Liver Metastases From Colorectal Cancer. Ann Surg 244, 254–259. 10.1097/01.sla.0000217629.94941.cf. [PubMed: 16858188]
4. Wood LD, Parsons DW, Jones S, Lin J, Sjoblom T, Leary RJ, et al. (2007). The Genomic Landscapes Of Human Breast And Colorectal Cancers. Science 318, 1108–1113. 10.1126/science.1145720. [PubMed: 17932254]
5. Li HT, Lu YY, An YX, Wang X, and Zhao QC (2011). Kras, Braf And Pik3ca Mutations In Human Colorectal Cancer: Relationship With Metastatic Colorectal Cancer. Oncol Rep 25, 1691–1697. 10.3892/or.2011.1217. [PubMed: 21424126]
6. Knijn N, Mekenkamp LJ, Klomp M, Vink–Borger ME, Tol J, Teerenstra S, et al. (2011). Kras Mutation Analysis: A Comparison Between Primary Tumours And Matched Liver Metastases In 305 Colorectal Cancer Patients. Br J Cancer 104, 1020–1026. 10.1038/bjc.2011.26. [PubMed: 21364579]
7. Boutin AT, Liao WT, Wang M, Hwang SS, Karpinets TV, Cheung H, et al. (2017). Oncogenic Kras Drives Invasion And Maintains Metastases In Colorectal Cancer. Genes Dev 31, 370–382. 10.1101/gad.293449.116. [PubMed: 28289141]
8. Liao W, Overman MJ, Boutin AT, Shang X, Zhao D, Dey P, et al. (2019). Kras–Irf2 Axis Drives Immune Suppression And Immune Therapy Resistance In Colorectal Cancer. Cancer Cell 35, 559–572 e557. 10.1016/j.ccell.2019.02.008. [PubMed: 30905761]

9. Spindler KL, Sorensen MM, Pallisgaard N, Andersen RF, Havelund BM, Ploen J, et al. (2013). Phase II Trial Of Temsirolimus Alone And In Combination With Irinotecan For KRAS Mutant Metastatic Colorectal Cancer: Outcome And Results Of KRAS Mutational Analysis In Plasma. Acta Oncol 52, 963–970. 10.3109/0284186X.2013.776175. [PubMed: 23514584]
10. Infante JR, Fecher LA, Falchook GS, Nallapareddy S, Gordon MS, Becerra C, et al. (2012). Safety, Pharmacokinetic, Pharmacodynamic, And Efficacy Data For The Oral Mek Inhibitor Trametinib: A Phase 1 Dose–Escalation Trial. Lancet Oncol 13, 773–781. 10.1016/S1470-2045(12)70270-X. [PubMed: 22805291]
11. Kopetz S, Grothey A, Yaeger R, Van Cutsem E, Desai J, Yoshino T, et al. (2019). Encorafenib, Binimetinib, And Cetuximab In Braf V600e–Mutated Colorectal Cancer. N Engl J Med 381, 1632–1643. 10.1056/NEJMoa1908075. [PubMed: 31566309]
12. Awad MM, Liu S, Rybkin II, Arbour KC, Dilly J, Zhu VW, Johnson ML, et al. (2021). Acquired Resistance To Kras(G12C) Inhibition In Cancer. N Engl J Med 384, 2382–2393. 10.1056/NEJMoa2105281. [PubMed: 34161704]
13. Bartoschek M, Oskolkov N, Bocci M, Lovrot J, Larsson C, Sommarin M, et al. (2018). Spatially And Functionally Distinct Subclasses Of Breast Cancer—Associated Fibroblasts Revealed By Single Cell Rna Sequencing. Nat Commun 9, 5150. 10.1038/s41467-018-07582-3. [PubMed: 30514914]
14. Bernard V, Semaan A, Huang J, San Lucas FA, Mulu FC, Stephens BM, et al. (2019). Single–Cell Transcriptomics Of Pancreatic Cancer Precursors Demonstrates Epithelial And Microenvironmental Heterogeneity As An Early Event In Neoplastic Progression. Clin Cancer Res 25, 2194–2205. 10.1158/1078-0432.CCR-18-1955. [PubMed: 30385653]
15. Costa A, Kieffer Y, Scholer–Dahirel A, Pelon F, Bourachot B, Cardon M, et al. (2018). Fibroblast Heterogeneity And Immunosuppressive Environment In Human Breast Cancer. Cancer Cell 33, 463–479 e410. 10.1016/j.ccell.2018.01.011. [PubMed: 29455927]
16. Li H, Courtois ET, Sengupta D, Tan Y, Chen KH, Goh JJL, et al. (2017). Reference Component Analysis Of Single–Cell Transcriptomes Elucidates Cellular Heterogeneity In Human Colorectal Tumors. Nat Genet 49, 708–718. 10.1038/ng.3818. [PubMed: 28319088]
17. El Agha E, Moiseenko A, Kheirollahi V, De Langhe S, Crnkovic S, Kwapiszewska G, et al. (2017). Two–Way Conversion Between Lipogenic And Myogenic Fibroblastic Phenotypes Marks The Progression And Resolution Of Lung Fibrosis. Cell Stem Cell 20, 261–273 e263. 10.1016/j.stem.2016.10.004. [PubMed: 27867035]
18. Shook BA, Wasko RR, Mano O, Rutenberg—Schoenberg M, Rudolph MC, Zirak B, et al. (2020). Dermal Adipocyte Lipolysis And Myofibroblast Conversion Are Required For Efficient Skin Repair. Cell Stem Cell 26, 880–895 e886. 10.1016/j.stem.2020.03.013. [PubMed: 32302523]
19. Biffi G, and Tuveson DA (2021). Diversity And Biology Of Cancer–Associated Fibroblasts. Physiol Rev 101, 147–176. 10.1152/physrev.00048.2019. [PubMed: 32466724]
20. Kalluri R (2016). The Biology And Function Of Fibroblasts In Cancer. Nat Rev Cancer 16, 582–598. 10.1038/nrc.2016.73. [PubMed: 27550820]
21. McAndrews KM, Vazquez–Arreguin K, Kwak C, Sugimoto H, Zheng X, Li B, et al. (2021). Alphasma(+) Fibroblasts Suppress Lgr5(+) Cancer Stem Cells And Restrain Colorectal Cancer Progression. Oncogene 40, 4440–4452. 10.1038/s41388-021-01866-7. [PubMed: 34108617]
22. Gong J, Lin Y, Zhang H, Liu C, Cheng Z, Yang X, et al. (2020). Reprogramming Of Lipid Metabolism In Cancer–Associated Fibroblasts Potentiates Migration Of Colorectal Cancer Cells. Cell Death Dis 11, 267. 10.1038/s41419-020-2434-z. [PubMed: 32327627]
23. Peng S, Li Y, Huang M, Tang G, Xie Y, Chen D, et al. (2022). Metabolomics Reveals That CAF–Derived Lipids Promote Colorectal Cancer Peritoneal Metastasis By Enhancing Membrane Fluidity. Int J Biol Sci 18, 1912–1932. 10.7150/ijbs.68484. [PubMed: 35342344]
24. Pereira BA, Vennin C, Papanicolaou M, Chambers CR, Herrmann D, Morton JP, et al. (2019). CAF Subpopulations: A New Reservoir Of Stromal Targets In Pancreatic Cancer. Trends Cancer 5, 724–741. 10.1016/j.trecan.2019.09.010. [PubMed: 31735290]
25. Wormann SM, Song L, Ai J, Diakopoulos KN, Kurkowski MU, Gorgulu K, Ruess D, et al. (2016). Loss Of P53 Function Activates JAK2–STAT3 Signaling To Promote Pancreatic Tumor Growth, Stroma Modification, And Gemcitabine Resistance In Mice And Is Associated With

Patient Survival. Gastroenterology 151, 180–193 e112. 10.1053/j.gastro.2016.03.010. [PubMed: 27003603]

26. Tape CJ, Ling S, Dimitriadi M, McMahon KM, Worboys JD, Leong HS, et al. (2016). Oncogenic KRAS Regulates Tumor Cell Signaling Via Stromal Reciprocation. Cell 165, 910–920. 10.1016/j.cell.2016.03.029. [PubMed: 27087446]
27. Velez-Delgado A, Donahue KL, Brown KL, Du W, Irizarry-Negron V, Menjivar RE, et al. (2022). Extrinsic KRAS Signaling Shapes the Pancreatic Microenvironment Through Fibroblast Reprogramming. Cell Mol Gastroenterol Hepatol 13, 1673–1699. 10.1016/j.jcmgh.2022.02.016. [PubMed: 35245687]
28. Shaashua L, Ben-Shmuel A, Pevsner-Fischer M, Friedman G, Levi-Galibov O, Nandakumar S, et al. (2022). BRCA mutational status shapes the stromal microenvironment of pancreatic cancer linking clusterin expression in cancer associated fibroblasts with HSF1 signaling. Nat Commun 13, 6513. 10.1038/s41467-022-34081-3. [PubMed: 36316305]
29. McGowan SE, and McCoy DM (2014). Regulation Of Fibroblast Lipid Storage And Myofibroblast Phenotypes During Alveolar Septation In Mice. Am J Physiol Lung Cell Mol Physiol 307, L618–631. 10.1152/ajplung.00144.2014. [PubMed: 25150063]
30. Park J, Ivey MJ, Deana Y, Riggsbee KL, Sorensen E, Schwabl V, et al. (2019). The Tcf21 Lineage Constitutes The Lung Lipofibroblast Population. Am J Physiol Lung Cell Mol Physiol 316, L872–L885. 10.1152/ajplung.00254.2018. [PubMed: 30675802]
31. Sanchez—Gurmaches J, Hung CM, and Guertin DA (2016). Emerging Complexities In Adipocyte Origins And Identity. Trends Cell Biol 26, 313–326. 10.1016/j.tcb.2016.01.004. [PubMed: 26874575]
32. Lavie D, Ben–Shmuel A, Erez N, and Scherz–Shouval R (2022). Cancer–Associated Fibroblasts In The Single–Cell Era. Nat Cancer 3, 793–807. 10.1038/s43018-022-00411-z. [PubMed: 35883004]
33. Deng CC, Hu YF, Zhu DH, Cheng Q, Gu JJ, Feng QL, et al. (2021). Single–Cell Rna–Seq Reveals Fibroblast Heterogeneity And Increased Mesenchymal Fibroblasts In Human Fibrotic Skin Diseases. Nat Commun 12, 3709. 10.1038/s41467-021-24110-y. [PubMed: 34140509]
34. Muhl L, Genove G, Leptidis S, Liu J, He L, Mocci G, et al. (2020). Single–Cell Analysis Uncovers Fibroblast Heterogeneity And Criteria For Fibroblast And Mural Cell Identification And Discrimination. Nat Commun 11, 3953. 10.1038/s41467-020-17740-1. [PubMed: 32769974]
35. Taylor CJ, Jetter C, et al. (2020). Single–Cell RNA Sequencing Reveals Profibrotic Roles Of Distinct Epithelial And Mesenchymal Lineages In Pulmonary Fibrosis. Sci Adv 6, eaba1972. 10.1126/sciadv.aba1972. [PubMed: 32832598]
36. Xie T, Wang Y, Deng N, Huang G, Taghavifar F, Geng Y, et al. (2018). Single–Cell Deconvolution Of Fibroblast Heterogeneity In Mouse Pulmonary Fibrosis. Cell Rep 22, 3625–3640. 10.1016/j.celrep.2018.03.010. [PubMed: 29590628]
37. Smith TM, Cong Z, Gilliland KL, Clawson GA, and Thiboutot DM (2006). Insulin–Like Growth Factor–1 Induces Lipid Production In Human SEB–1 Sebocytes Via Sterol Response Element–Binding Protein–1. J Invest Dermatol 126, 1226–1232. 10.1038/sj.jid.5700278. [PubMed: 16575389]
38. Cordero AD, Callihan EC, Said R, Alowais Y, Paffhausen ES, and Bracht JR (2020). Epigenetic Regulation of Neuregulin-1 Tunes White Adipose Stem Cell Differentiation. Cells 9(5):1148. 10.3390/cells9051148. [PubMed: 32392729]
39. Han X, Zhang Z, He L, Zhu H, Li Y, Pu W, et al. (2021). A Suite Of New Dre Recombinase Drivers Markedly Expands The Ability To Perform Intersectional Genetic Targeting. Cell Stem Cell 28, 1160–1176 e1167. 10.1016/j.stem.2021.01.007. [PubMed: 33567267]
40. Lin X, Dong R, Diao S, Yu G, Wang L, Li J, et al. (2017). Sfrp2 Enhanced The Adipogenic And Neuronal Differentiation Potentials Of Stem Cells From Apical Papilla. Cell Biol Int 41, 534–543. 10.1002/cbin.10757. [PubMed: 28244619]
41. Ullah M, Stich S, Haupl T, Eucker J, Sittinger M, and Ringe J (2013). Reverse differentiation as a gene filtering tool in genome expression profiling of adipogenesis for fat marker gene selection and their analysis. PLoS One 8, e69754. 10.1371/journal.pone.0069754. [PubMed: 23922792]

42. Guan H, Zhang Y, Gao S, Bai L, Zhao S, Cheng XW, Fan J, and Liu E (2018). Differential Patterns of Secreted Frizzled-Related Protein 4 (SFRP4) in Adipocyte Differentiation: Adipose Depot Specificity. Cell Physiol Biochem 46, 2149–2164. 10.1159/000489545. [PubMed: 29730658]
43. Franzen O, Gan LM, and Bjorkegren JLM (2019). Panglaodb: A Web Server For Exploration Of Mouse And Human Single–Cell Rna Sequencing Data. Database (Oxford) 2019;2019:baz046. 10.1093/database/baz046. [PubMed: 30951143]
44. Goralski KB, McCarthy TC, Hanniman EA, Zabel BA, Butcher EC, Parlee SD, et al. (2007). Chemerin, A Novel Adipokine That Regulates Adipogenesis And Adipocyte Metabolism. J Biol Chem 282, 28175–28188. 10.1074/jbc.M700793200. [PubMed: 17635925]
45. Unamuno X, Gomez–Ambrosi J, Ramirez B, Rodriguez A, Becerril S, Valenti V, et al. (2020). Dermatopontin, A Novel Adipokine Promoting Adipose Tissue Extracellular Matrix Remodelling And Inflammation In Obesity. J Clin Med 9. 10.3390/jcm9041069.
46. Christodoulides C, Lagathu C, Sethi JK, and Vidal–Puig A (2009). Adipogenesis And Wnt Signalling. Trends Endocrinol Metab 20, 16–24. 10.1016/j.tem.2008.09.002. [PubMed: 19008118]
47. Huang H, Song TJ, Li X, Hu L, He Q, Liu M, et al. (2009). Bmp Signaling Pathway Is Required For Commitment Of C3h10t1/2 Pluripotent Stem Cells To The Adipocyte Lineage. Proc Natl Acad Sci U S A 106, 12670–12675. 10.1073/pnas.0906266106. [PubMed: 19620713]
48. Lv YQ, Dhlamini Q, Chen C, Li X, Bellusci S, and Zhang JS (2021). Fgf10 And Lipofibroblasts In Lung Homeostasis And Disease: Insights Gained From The Adipocytes. Front Cell Dev Biol 9, 645400. 10.3389/fcell.2021.645400. [PubMed: 34124037]
49. Cristancho AG, and Lazar MA (2011). Forming Functional Fat: A Growing Understanding Of Adipocyte Differentiation. Nat Rev Mol Cell Biol 12, 722–734. 10.1038/nrm3198. [PubMed: 21952300]
50. Banerjee S, Zhang X, Kuang S, Wang J, Li L, Fan G, et al. (2021). Comparative analysis of clonal evolution among patients with right- and left-sided colon and rectal cancer. iScience 24, 102718. 10.1016/j.isci.2021.102718. [PubMed: 34258553]
51. Cellurale C, Sabio G, Kennedy NJ, Das M, Barlow M, Sandy P, et al. (2011). Requirement of c-Jun NH(2)-terminal kinase for Ras-initiated tumor formation. Mol Cell Biol 31, 1565–1576. 10.1128/MCB.01122-10. [PubMed: 21282468]
52. Reed BC, and Lane MD (1980). Insulin Receptor Synthesis And Turnover In Differentiating 3T3–L1 Preadipocytes. Proc Natl Acad Sci U S A 77, 285–289. 10.1073/pnas.77.1.285. [PubMed: 6928620]
53. Muzny DM, Bainbridge MN, Chang K, Dinh HH, Drummond JA, Fowler G, et al. (2012). Comprehensive Molecular Characterization Of Human Colon And Rectal Cancer. Nature 487, 330–337. 10.1038/nature11252. [PubMed: 22810696]
54. Fechner PY (1996). The Role Of Sry In Mammalian Sex Determination. Acta Paediatr Jpn 38, 380–389. 10.1111/j.1442-200x.1996.tb03512.x. [PubMed: 8840551]
55. Volker JL, Rameh LE, Zhu Q, DeCaprio J, and Hansen U (1997). Mitogenic Stimulation Of Resting T Cells Causes Rapid Phosphorylation Of The Transcription Factor LSF And Increased DNA–Binding Activity. Genes Dev 11, 1435–1446. 10.1101/gad.11.11.1435. [PubMed: 9192871]
56. Grant TJ, Bishop JA, Christadore LM, Barot G, Chin HG, Woodson S, et al. (2012). Antiproliferative Small–Molecule Inhibitors Of Transcription Factor Lsf Reveal Oncogene Addiction To Lsf In Hepatocellular Carcinoma. Proc Natl Acad Sci U S A 109, 4503–4508. 10.1073/pnas.1121601109. [PubMed: 22396589]
57. Santhekadur PK, Rajasekaran D, Siddiq A, Gredler R, Chen D, Schaus SE, et al. (2012). The Transcription Factor LSF: A Novel Oncogene For Hepatocellular Carcinoma. Am J Cancer Res 2, 269–285. [PubMed: 22679558]
58. Kaplan NB, Grant MM, and Brody JS (1985). The Lipid Interstitial Cell Of The Pulmonary Alveolus. Age And Species Differences. Am Rev Respir Dis 132, 1307–1312. 10.1164/arrd.1985.132.6.1307. [PubMed: 3000236]
59. O'Hare KH, and Sheridan MN (1970). Electron Microscopic Observations On The Morphogenesis Of The Albino Rat Lung, With Special Reference To Pulmonary Epithelial Cells. Am J Anat 127, 181–205. 10.1002/aja.1001270205. [PubMed: 5413181]

60. Barkauskas CE, Cronce MJ, Rackley CR, Bowie EJ, Keene DR, Stripp BR, et al. (2013). Type 2 Alveolar Cells Are Stem Cells In Adult Lung. J Clin Invest 123, 3025–3036. 10.1172/JCI68782. [PubMed: 23921127]
61. McQualter JL, McCarty RC, Van der Velden J, O'Donoghue RJ, Asselin–Labat ML, Bozinovski S, et al. (2013). Tgf–Beta Signaling In Stromal Cells Acts Upstream Of Fgf–10 To Regulate Epithelial Stem Cell Growth In The Adult Lung. Stem Cell Res 11, 1222–1233. 10.1016/j.scr.2013.08.007. [PubMed: 24029687]
62. Rehan VK, and Torday JS (2014). The Lung Alveolar Lipofibroblast: An Evolutionary Strategy Against Neonatal Hyperoxic Lung Injury. Antioxid Redox Signal 21, 1893–1904. 10.1089/ars.2013.5793. [PubMed: 24386954]
63. Ntokou A, Klein F, Dontireddy D, Becker S, Bellusci S, Richardson WD, et al. (2015). Characterization Of The Platelet–Derived Growth Factor Receptor–Alpha–Positive Cell Lineage During Murine Late Lung Development. Am J Physiol Lung Cell Mol Physiol 309, L942–958. 10.1152/ajplung.00272.2014. [PubMed: 26320158]
64. Accioly MT, Pacheco P, Maya-Monteiro CM, Carrossini N, Robbs BK, Oliveira SS, et al. (2008). Lipid bodies are reservoirs of cyclooxygenase-2 and sites of prostaglandin-E2 synthesis in colon cancer cells. Cancer Res 68, 1732–1740. 10.1158/0008-5472.CAN-07-1999. [PubMed: 18339853]
65. Pai R, Szabo IL, Soreghan BA, Atay S, Kawanaka H, and Tarnawski AS (2001). PGE(2) stimulates VEGF expression in endothelial cells via ERK2/JNK1 signaling pathways. Biochem Biophys Res Commun 286, 923–928. 10.1006/bbrc.2001.5494. [PubMed: 11527387]
66. Prescott SM (2000). Is cyclooxygenase-2 the alpha and the omega in cancer? J Clin Invest 105, 1511–1513. 10.1172/JCI10241. [PubMed: 10841506]
67. Zhang X, Sun F, Qiao Y, Zheng W, Liu Y, Chen Y, et al. (2017). TFCP2 Is Required For YAP–Dependent Transcription To Stimulate Liver Malignancy. Cell Rep 21, 1227–1239. 10.1016/j.celrep.2017.10.017. [PubMed: 29091762]
68. Shao K, Pu W, Zhang J, Guo S, Qian F, Glurich I, et al. (2021). DNA Hypermethylation Contributes To Colorectal Cancer Metastasis By Regulating The Binding Of CEBPB And TFCP2 To The CPEB1 Promoter. Clin Epigenetics 13, 89. 10.1186/s13148-021-01071-z. [PubMed: 33892791]
69. Rajasekaran D, Siddiq A, Willoughby JL, Biagi JM, Christadore LM, Yunes SA, et al. (2015). Small Molecule Inhibitors Of Late SV40 Factor (LSF) Abrogate Hepatocellular Carcinoma (HCC): Evaluation Using An Endogenous HCC Model. Oncotarget 6, 26266–26277. 10.18632/oncotarget.4656. [PubMed: 26313006]
70. Scott MA, Nguyen VT, Levi B, and James AW (2011). Current Methods Of Adipogenic Differentiation Of Mesenchymal Stem Cells. Stem Cells Dev 20, 1793–1804. 10.1089/scd.2011.0040. [PubMed: 21526925]
71. Labun K, Montague TG, Krause M, Torres Cleuren YN, Tjeldnes H, and Valen E (2019). Chopchop V3: Expanding The Crispr Web Toolbox Beyond Genome Editing. Nucleic Acids Res 47, W171–W174. 10.1093/nar/gkz365. [PubMed: 31106371]
72. Sanjana NE, Shalem O, and Zhang F (2014). Improved Vectors And Genome–Wide Libraries For CRISPR Screening. Nat Methods 11, 783–784. 10.1038/nmeth.3047. [PubMed: 25075903]
73. Crowe AR, and Yue W (2019). Semi-quantitative Determination of Protein Expression using Immunohistochemistry Staining and Analysis: An Integrated Protocol. Bio Protoc 9,24: e3465. doi:10.21769/BioProtoc.3465
74. Schindelin J, Arganda-Carreras I, Frise E, Kaynig V, Longair M, Pietzsch T, et al. (2012). Fiji: an open-source platform for biological-image analysis. Nature Methods, 9(7), 676–682. doi:10.1038/nmeth.2019 [PubMed: 22743772]
75. Schneider CA, Rasband WS, & Eliceiri KW (2012). NIH Image to ImageJ: 25 years of image analysis. Nature Methods, 9(7), 671–675. doi:10.1038/nmeth.2089 [PubMed: 22930834]
76. Khan M, and Gasser S (2016). Generating Primary Fibroblast Cultures from Mouse Ear and Tail Tissues. J Vis Exp. 10;(107):53565. doi: 10.3791/53565.
77. Boroujerdi A, Tigges U, Welser-Alves JV, and Milner R (2014). Isolation and culture of primary pericytes from mouse brain. Methods Mol Biol 1135, 383–392. 10.1007/978-1-4939-0320-7_31. [PubMed: 24510880]

78. Terranova C, Tang M, Orouji E, Maitituoheti M, Raman A, Amin S, et al. (2018). An Integrated Platform For Genome–Wide Mapping Of Chromatin States Using High–Throughput Chip–Sequencing In Tumor Tissues. J Vis Exp. 5;(134):56972. 10.3791/56972.

79. Perez LJ, Rios L, Trivedi P, D'Souza K, Cowie A, Nzirorera C, et al. (2017). Validation Of Optimal Reference Genes For Quantitative Real Time PCR In Muscle And Adipose Tissue For Obesity And Diabetes Research. Sci Rep 7, 3612. 10.1038/s41598-017-03730-9. [PubMed: 28620170]

SIGNIFICANCE

This study identified a molecular mechanism contributing to KRAS*–driven CRC progression via fibroblast transformation in the tumor microenvironment to produce VEGFA driving tumor angiogenesis. In preclinical models, targeting the KRAS*–TFCP2–VEGFA axis impaired tumor progression, revealing a potential novel therapeutic option for patients with KRAS*–driven CRC.

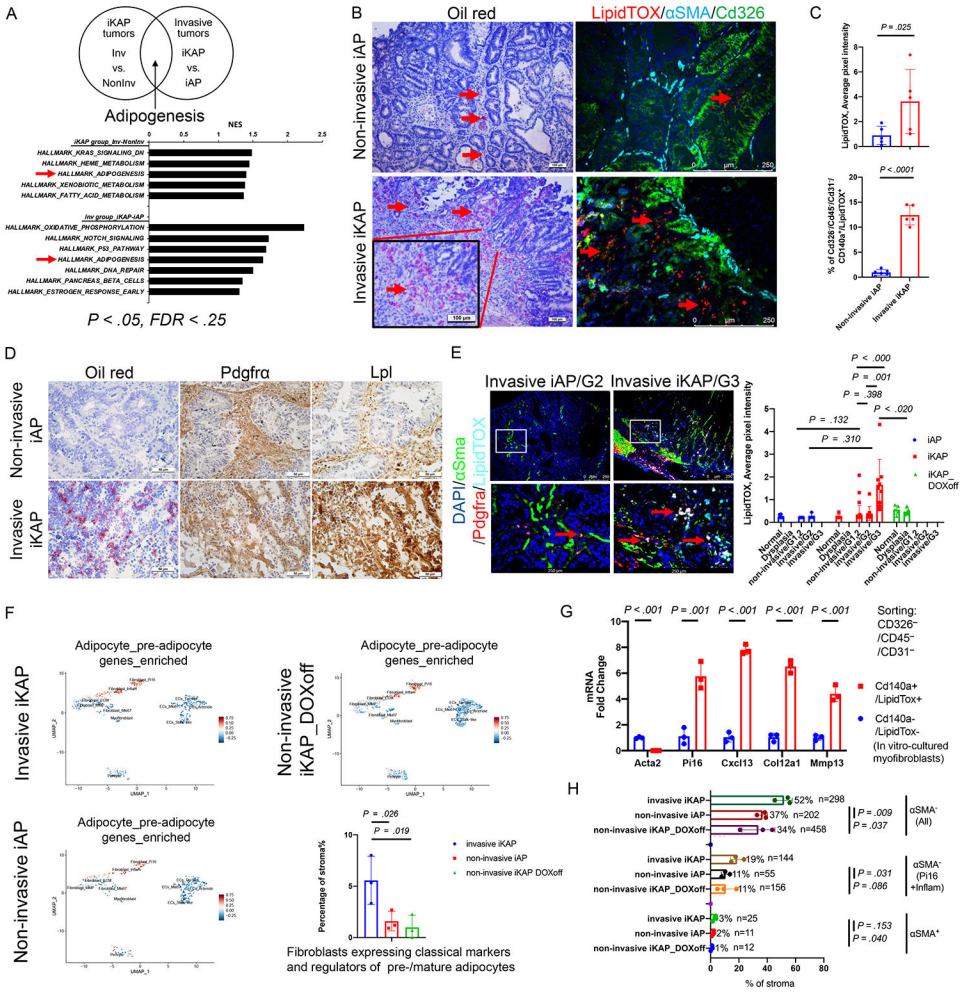

Figure 1. Lipid–rich CAFs are enriched in Kras* colorectal cancer stroma.

(A) GSEA transcriptomic profiling of iKAP vs. iAP tumors and invasive (Inv) vs. noninvasive (NonInv) tumors shows enriched hallmark pathways. N ≥ 4. Please see Methods “RNA sequencing and analysis” for details of sample collection and characterization of KRAS wild type, KRAS mutation, invasive and non–invasive tumors. Red arrows indicate the adipogenesis pathway. NES, normalized enrichment score.

(B) Immunohistochemical staining of lipid droplets (oil red) and immunofluorescence staining of lipid droplets (LipidTOX), CD326 and αSMA in colorectal cancer (CRC) tumors from invasive iKAP and non-invasive iAP genetically engineered mouse (GEM) models. Please see Methods for details of sample collection of invasive iKAP and non–invasive iAP tumors. Red arrows indicate lipid droplets. Scale bar, 100 μm and 250 μm; N = 6 biological replicates.

(C) The quantification of LipidTOX staining intensity in non-invasive iAP and invasive iKAP tumors (upper panel). N = 5 biological replicates. The percentages of CD326⁻/CD45⁻/CD31⁻/CD140a+/LipidTOX+ cells in non–invasive iAP and invasive iKAP tumors determined using flow cytometry analysis (lower panel). N = 5 biological replicates. Data represent mean ± SD. Student's t test.

(D) Immunohistochemical analysis of lipid droplets, non-myofibroblast (PDFGRα) and adipocyte (LPL) genes in CRC tumors from invasive iKAP and non–invasive iAP GEM models. Scale bar, 50 μm; N = 3 biological replicates.

(E) Immunofluorescence staining of lipid droplets, αSMA, and PDGFRα in moderate grade (G2) and high grade (G3) invasive iKAP and iAP tumors (grade scored by GI pathologist; blinded) (left panel). White rectangles indicate the enlarged area presented in the lower images. Red arrows indicate the co-staining of PDGFRα and lipid droplet. Scale bar, 250 μm. Quantification of LipidTOX at different tumor status (right panel). N ≥ 3 biological replicates. Data represent mean ± SD. Student's t test.

(F) Adipocyte and pre-adipocyte genes' module score plots of invasive iKAP, non-invasive iAP, and non-invasive iKAP_DOXoff tumor stroma subgroups as determined using the Seurat's AddModuleScore function. Please see Methods "Single cell RNA sequencing and analysis of mouse and human CRC" for details of obtaining module score plots. The percentage of fibroblasts that express classical markers and regulators of pre-/mature adipocytes in tumor stroma (lower right panel). N = 3 biological replicates. Data represent mean ± SD. Student's t test.

(G) CAF marker gene expression levels in $CD326^{-}/CD45^{-}/CD31^{-}/PDGFR\alpha^{+}/LipidTOX^{+}$–sorted cells and $CD326^{-}/CD45^{-}/CD31^{-}/PDGFR\alpha^{+}/LipidTOX^{-}$ –sorted/cultured myofibroblasts. See Methods for lipid–rich fibroblasts and lipid–sparse fibroblasts (myofibroblasts) collection. N = 3 biological replicates. Data represent mean ± SD. Student's t test.

(H) Proportion of αSMA^{-} lipid–rich CAF subgroups (the combination of 4 αSMA^{-} CAF subgroups, the combination of inflammatory and $PI16^{+}$ CAF subgroups, and αSMA+ myofibroblasts) in invasive iKAP, non-invasive iAP, and non-invasive iKAP_DOXoff tumor stroma cells. N = 3 biological replicates. Data represent mean ± SD. Student's t test.

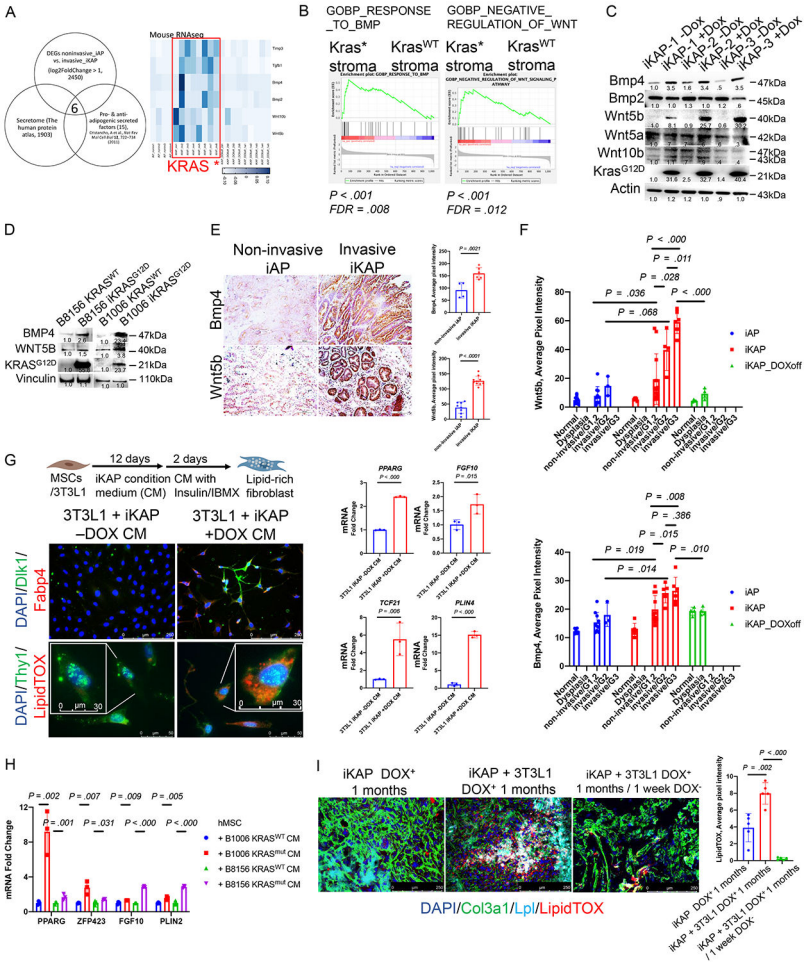

Figure 2. Kras* upregulates proadipogenic cytokines and drives lipofibrogenesis.

(A) Venn diagram of the putative secretome that is regulated by KRAS* and modulates adipogenesis (left panel). Heatmap representation of the pro- and anti-adipogenic cytokine candidate gene expression in iAP, iKAP, and iKAP_DOXoff colorectal cancer (CRC) in the bulk RNA sequencing data set. Blue and white indicate high and low expression, respectively. The red rectangle represents the iKAP group with high expression of pro- and anti-adipogenic cytokine genes.

(B) GSEA enrichment plots showing the negative regulation of Wnt and the response to Bmp4 signaling in an scRNAseq data set from iKAP and iKAP_DOXoff CRC tumor stroma. FDR, false discovery rate; GOBP, Gene Ontology Biological Process; WT, wild type.

(C) Immunoblots of Bmp and Wnt family proteins in the cell lysates of iKAP cell lines with or without DOX supplementation to express Kras*.

(D) Immunoblots of BMP4 and WNT5B in the cell lysates of 2 PDXOs (B8156 and B1006) with or without DOX supplementation to induce $KRAS^{G12D}$ expression.

(E) Immunohistochemical staining (left panel) and quantification (right panel) of Wnt5b and Bmp4 in non-invasive iAP and invasive iKAP tumors. Scale bar, 100 μm; n ≥ 4 biological replicates. Data represent mean ± SD. Student's t test.

(F) Quantification of Wnt5b and Bmp4 expression levels in high–, moderate– and low–grade invasive and non–invasive iKAP and iAP tumors (grade scored by GI pathologist; blinded). N ≥ 3 biological replicates. Data represent mean ± SD. Student's t test.

(G) Schematic diagram of CM co-cultured experiments (upper panel) to demonstrate the impact of iKAP CM on lipid-rich fibroblast differentiation. (See Methods for cell culture details.) Immunofluorescence staining of lipid droplets, THY1, and DLK1 (lower panel) and quantification of lipid–rich CAF genes using quantitative reverse transcription polymerase chain reaction (RT–qPCR; right panel) in iKAP conditioned medium (CM)–educated 3T3L1 cells. Scale bar, 250 μm, 50 μm, and 30 μm; n = 3 biological replicates. IBMX, 3–isobutyl–1–methylxanthine; MSCs, mesenchymal stem cells. Data represent mean ± SD. Student's t test.

(H) RT–qPCR quantification of lipid–rich CAF genes in PDXO Kras* CM–educated hMSCs. N = 3 biological replicates. Data represent mean ± SD. Student's t test.

(I) Immunofluorescence analysis of lipid droplets, Col3a1, and Lpl in subcutaneous iKAP tumors and tumors generated by co–injecting iKAP cell lines and 3T3L1 into nude mice. Scale bar, 250 μm. Quantification of LipidTOX intensity (right panel). N = 5 biological replicates. Data represent mean ± SD. Student's t test.

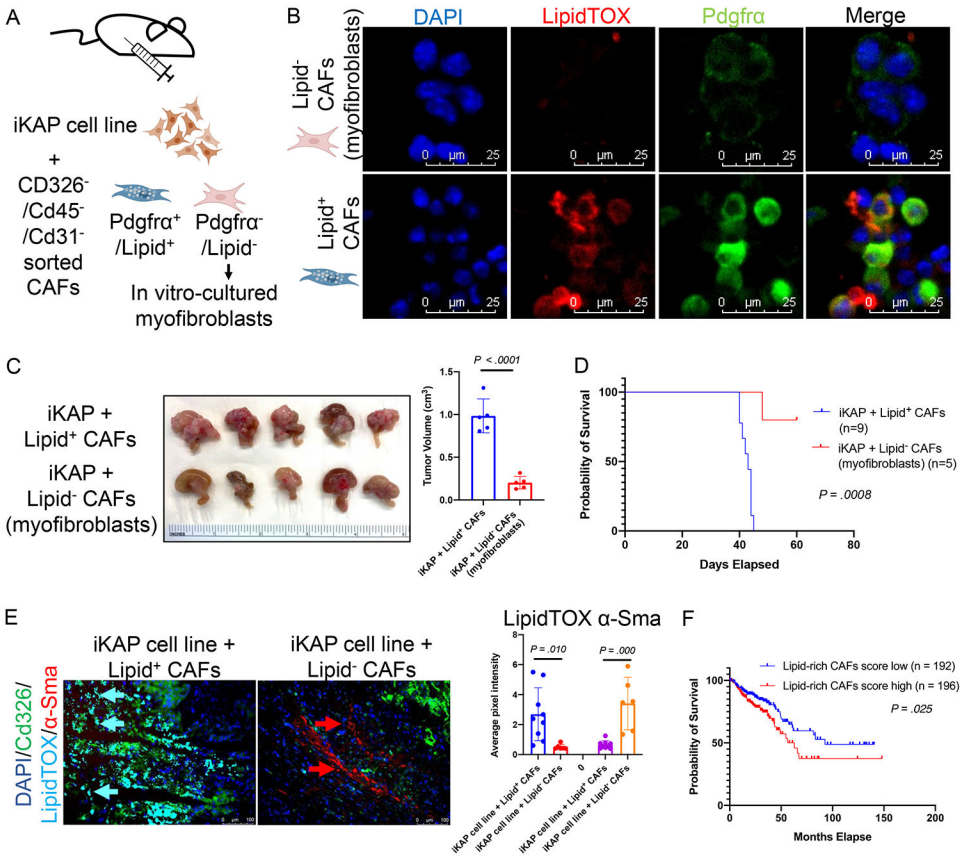

Figure 3. Lipid–rich CAFs drive tumor progression.

(A) Schematic diagram of orthotopic co–injection experiments in mice. See Methods “Flow cytometry and sorting” for details.

(B) Immunofluorescence staining of lipid droplets and PDGFRα in Lipid+ CAFs ($CD326^{-}/CD45^{-}/CD31^{-}$, $PDGFR\alpha^{+}/LipidTOX^{+}$ sorted cells) and Lipid- CAFs ($PDGFR\alpha^{-}/LipidTOX^{-}$ sorted and cultured cells). N = 6 biological replicates. CAFs, cancer–associated fibroblasts.

(C) Tumors generated by orthotopic co–injection in cecum of lipid–rich CAFs or lipid–sparse CAFs (myofibroblasts) with iKAP cell line (left panel) at 4 weeks. Quantification of tumor size (right panel). N = 5 biological replicates. Data represent mean ± SD. Student's t test.

(D) Orthotopic co-injection of lipid–rich CAFs and the iKAP cell line decreases overall survival in mice. N ≥ 5 biological replicates. Log–rank (Mantel–Cox) test.

(E) Immunofluorescence staining of lipid droplets, αSMA, and CD326 in tumors shown in Fig. 3C (left panel). Quantification of LipidTOX and αSMA (right panel). N ≥ 5 biological replicates. Data represent mean ± SD. Student's t test.

(F) Survival of colorectal cancer patients with high vs. low gene set variation analysis scores for lipid–rich CAF gene signatures (data from The Cancer Genome Atlas– Colon adenocarcinoma). See Supplementary Table S2 for Lipid–rich CAF gene signatures. The median lipid-rich CAF GSVA score was used as cut-off to define high and low groups. Log–rank (Mantel–Cox) test.

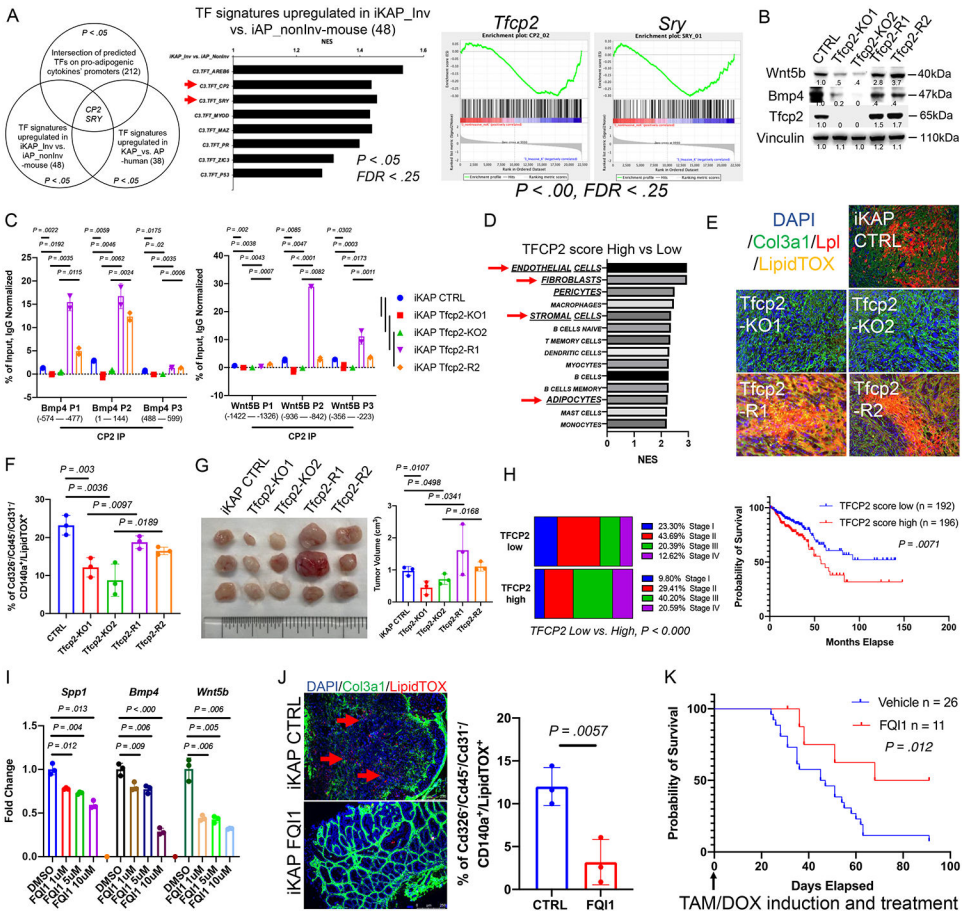

Figure 4. KRAS* regulates pro–adipogenesis cytokines through TFCP2.

(A) Venn diagram of the putative transcription factors (TFs) that bind to the consensus motifs on promoters of pro–adipogenic cytokines as well as candidates from GSEA of TF signatures enriched in KRAS* tumors (left panel). The gene lists of these 3 datasets are provided in Supplementary Table S3. The TF signatures enriched in KRAS* tumors in a genetically engineered mouse (GEM) model (middle panel). Enrichment plot of *TFCP2* and *SRY* gene signatures in iKAP tumors (right panel). *CP2, TFCP2*; FDR, false discovery rate.

(B) Immunoblots of pro–adipogenic cytokines BMP4 and WNT5B, and TFCP2 in TFCP2–knockout and rescued iKAP cell lines.

(C) Chromatin immunoprecipitation–quantitative polymerase chain reaction (ChIP–qPCR) analysis of WNT5B and BMP4 promoter sequences on the TFCP2 binding elements. N = 3 biological replicates. Data represent mean ± SD. Student's t test.

(D) Cell type correlations in high TFCP2–regulated gene signature (GSEA, C3 TFT) gene set variation analysis (GSVA) scores of TCGA–COAD patient cohort. NES, normalized enrichment score.

(E) Immunofluorescence staining of lipid droplets, LPL, and COL3a1 in TFCP2–knockout and rescued tumors. Scale bar, 100 μm; n = 5 biological replicates.

(F) Percentages of $CD326^{-}/CD45^{-}/CD31^{-}/CD140a^{+}/LipidTOX^{+}$ –sorted cells in TFCP2–knockout and rescued tumors from Fig. 4E. N = 3 biological replicates. Data represent mean ± SD. Student's t test.

(G) Tumors generated by xenograft implantation of TFCP2–knockout and rescued iKAP cell lines into nude mice in 1 month (left panel). Quantification of tumor burdens (right panel). N = 3 biological replicates. Data represent mean ± SD. Student's t test.

(H) TCGA–COAD tumor stages and survival in high vs. low GSVA scores of TFCP2–regulated gene signatures. The median TFCP2 GSVA score was used as cut-off to define high and low groups. Chi-square test for tumor stages and Log–rank (Mantel–Cox) test for survival analyses.

(I) RT–qPCR validation of pro–adipogenic cytokine genes in FQI1–treated iKAP cell lines in vitro. N = 3 biological replicates. Data represent mean ± SD. Student's t test.

(J) Immunofluorescence staining of lipid droplets and Col3a1 (left panel) and percentages of $CD326^{-}/CD45^{-}/CD31^{-}/CD140a^{+}/LipidTOX^{+}$ –sorted cells in FQI1–treated iKAP tumors (right panel). Scale bar, 250 μm; N = 3 biological replicates. Data represent mean ± SD. Student's t test.

(K) Kaplan–Meier survival curves of iKAP mice treated with FQI1 or vehicle. TAM, tamoxifen. Log–rank (Mantel–Cox) test.

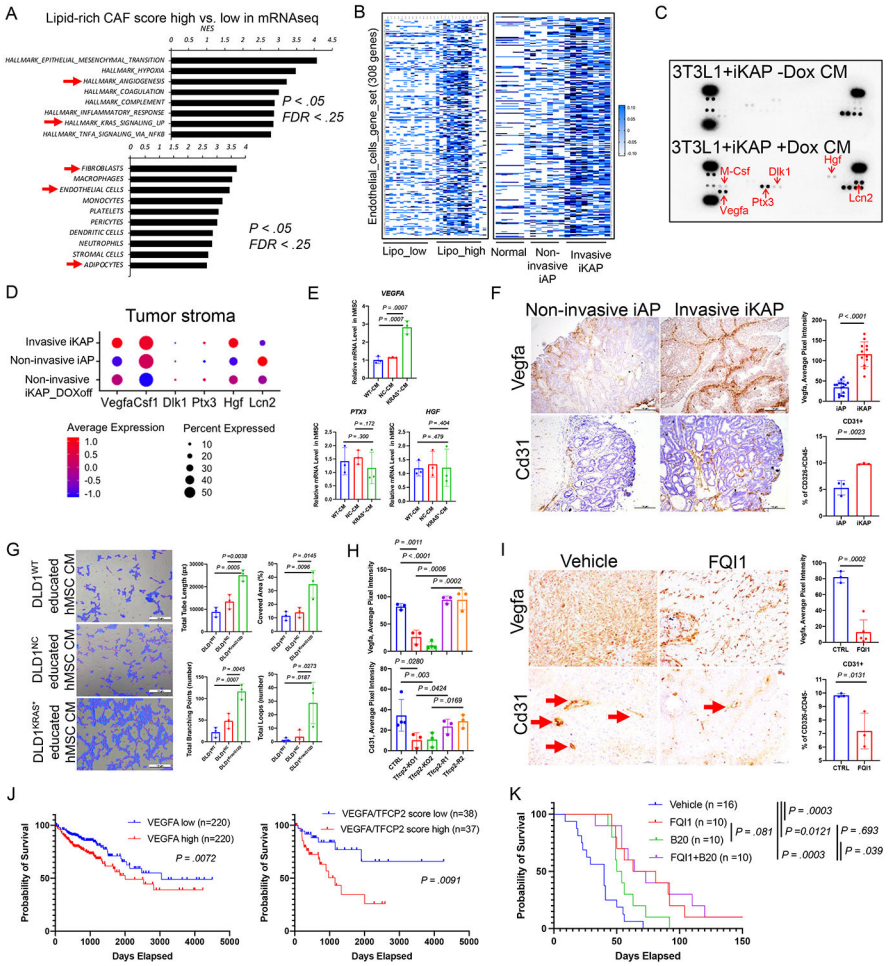

Figure 5. Lipid–rich CAFs secrete VEGFA to promote tumor angiogenesis.

(A) Transcriptomic profiling of high vs. low gene set variation analysis (GSVA) scores of lipid–rich CAF gene signatures in mouse bulk RNA sequencing dataset. Upper panel shows the enriched hallmark pathways and lower panel shows the correlated cell types in KRAS* tumors as determined by GSEA. FDR, false discovery rate.

(B) Heatmap representation the expression of the endothelial cell gene set in high vs. low lipid–rich CAF GSVA scores in mouse bulk tumor RNA sequencing dataset (left panel). Expression of the endothelial cell gene set in non-invasive iAP vs invasive iKAP bulk tumor RNA sequencing dataset (right panel). Blue and white indicate high and low expression, respectively.

(C) Adipokine array of cell lysates from Kras*(+DOX)– and $Kras^{wt}$(−DOX)– conditioned medium (CM)–educated embryonic fibroblasts (3T3L1).

(D) Adipokine candidate gene expression in the stroma of iKAP, iAP, and iKAP_DOX–off tumors using scRNA–seq. The average expression color scale was from 1 to −1. The dot size represents the proportion of expressing cells in each group. N = 3 biological replicates.

(E) RT–qPCR validation of targeted adipokines, VEGFA, PTX3 and HGF, in $DLD1^{KRASG12D}$ CM–educated hMSCs. N = 3 biological replicates. Data represent mean ± SD. Student's t test.

(F) Immunohistochemical staining of VEGFA and CD31 in iAP and iKAP tumors. Representative images (left) and quantification (upper right). Scale bar, 100 μm; N ≥ 3 biological replicates. Flow analysis of $CD326^{-}/CD45^{-}/CD31^{+}$ endothelial cells in iAP and iKAP tumors (lower right). N = 3 biological replicates. Data represent mean ± SD. Student's t test.

(G) The tube or capillary–like shapes of the HUVEC co-cultured with CM of $DLD1^{KRASG12D}$ CM–educated hMSCs. See Methods "Angiogenesis assay" for details. Representative images (left) and quantification (right). Scale bar, 100 μm; N = 3 biological replicates. Data represent mean ± SD. Student's t test.

(H) Immunohistochemical staining of VEGFA and CD31 in TFCP2–knockout and rescued iKAP tumors. N ≥ 3 biological replicates. Data represent mean ± SD. Student's t test.

(I) Immunohistochemical staining of VEGFA and CD31 in FQI1–treated iKAP tumors. Representative images (left) and quantification (upper right). Scale bar, 50 μm; N = 3 biological replicates. Flow analysis of $CD326^{-}/CD45^{-}/CD31^{+}$ endothelial cells in FQI1–treated iKAP tumors (lower right). N = 3 biological replicates.

(J) Kaplan–Meier survival curves of high vs. low VEGFA expression (left) and high vs. low VEGFA expression plus TFCP2 GSVA score (right) in TCGA-COAD data from cBioPortal. VEGF high and low were defined using 50% cut-off of the RNA expression levels. VEGF/TFCP2 GSVA score ≥ 4^{th} quantile was defined as high group and ≤ 1^{st} quantile as low group. Log–rank (Mantel–Cox) test.

(K) Kaplan–Meier survival curves of iKAP mice treated with FQI1 and/or Vegfa monoclonal antibody treatment (single and combination). Log–rank (Mantel–Cox) test.